Monthly Notices of the ROYAL ASTRONOMICAL SOCIETY

MNRAS **520,** 4037–4056 (2023) https://doi.org/10.1093/mnras/stad387
Advance Access publication 2023 February 8

Spectroscopy of CASSOWARY gravitationally lensed galaxies in SDSS: characterization of an extremely bright reionization-era analogue at $z = 1.42$

Ramesh Mainali [1,2,3★] Daniel P. Stark,[2] Tucker Jones [4] Richard S. Ellis,[5] Yashar D. Hezaveh[6,7] and Jane R. Rigby[1]

[1]*Observational Cosmology Lab, NASA Goddard Space Flight Center, Greenbelt, MD 20771, USA*
[2]*Steward Observatory, University of Arizona, 933 N Cherry Ave, Tucson, AZ 85719, USA*
[3]*Department of Physics, The Catholic University of America, Washington, DC 20064, USA*
[4]*Department of Physics, University of California Davis, 1 Shields Avenue, Davis, CA 95616, USA*
[5]*Department of Physics and Astronomy, University College London, Gower Street, London WC1E 6BT, UK*
[6]*Center for Computational Astrophysics, Flatiron Institute, 162 Fifth Avenue, New York, NY 10010, USA*
[7]*Département de Physique, Université de Montréal, Montreal, QC H3T 1J4, Canada*

Accepted 2023 January 26. Received 2023 January 26; in original form 2022 July 8

ABSTRACT

We present new observations of 16 bright ($r = 19$–21) gravitationally lensed galaxies at $z \simeq 1$–3 selected from the CASSOWARY survey. Included in our sample is the $z = 1.42$ galaxy CSWA-141, one of the brightest known reionization-era analogues at high redshift (g = 20.5), with a large specific star formation rate (31.2 Gyr^{-1}) and an [O III]+Hβ equivalent width ($EW_{[O\,III]+H\beta}$ = 730 Å) that is nearly identical to the average value expected at $z \simeq 7$–8. In this paper, we investigate the rest-frame UV nebular line emission in our sample with the goal of understanding the factors that regulate strong C III] emission. Although most of the sources in our sample show weak UV line emission, we find elevated C III] in the spectrum of CSWA-141 ($EW_{C\,III]}$ = 4.6 ± 1.9 Å) together with detections of other prominent emission lines (O III], Si III], Fe II*, Mg II). We compare the rest-optical line properties of high-redshift galaxies with strong and weak C III] emission, and find that systems with the strongest UV line emission tend to have young stellar populations and nebular gas that is moderately metal-poor and highly ionized, consistent with trends seen at low and high redshift. The brightness of CSWA-141 enables detailed investigation of the extreme emission line galaxies which become common at $z > 6$. We find that gas traced by the C III] doublet likely probes higher densities than that traced by [O II] and [S II]. Characterization of the spectrally resolved Mg II emission line and several low-ionization absorption lines suggests neutral gas around the young stars is likely optically thin, potentially facilitating the escape of ionizing radiation.

Key words: galaxies: evolution – galaxies: formation – galaxies: high-redshift.

1 INTRODUCTION

Over the last decade, much progress has been made in our understanding of galaxies in the first billion years of cosmic time (for a review, see Stark 2016). Deep infrared imaging has uncovered thousands of photometrically selected star-forming systems thought to lie in the redshift range $6 < z < 9$ (e.g. McLure et al. 2013; Bouwens et al. 2015, 2021; Finkelstein et al. 2015; Livermore, Finkelstein & Lotz 2017; Ishigaki et al. 2018), providing a census of UV-selected galaxies throughout the reionization era. The spectral energy distributions (SEDs) point towards a population undergoing rapid stellar mass growth with blue UV continuum spectral slopes (e.g. Rogers, McLure & Dunlop 2013; Bouwens et al. 2014), low stellar masses, and large specific star formation rates (sSFR; Stark et al. 2013b; González et al. 2014; Grazian et al. 2015; Salmon et al. 2015; Curtis-Lake et al. 2016).

In the last 5 yr, our first constraints on the nebular emission properties of galaxies at these early epochs have emerged. *Spitzer*/IRAC photometry suggests that nearly half of the UV-selected galaxies at $z \simeq 7$ have extremely large [O III]+Hβ equivalent widths (EWs) (Labbé et al. 2013; Smit et al. 2014, 2015; Roberts-Borsani et al. 2016; De Barros et al. 2017; Endsley et al. 2021), indicating that very recent ($\lesssim$50 Myr) activity powers the UV and optical luminosity, as expected for galaxies undergoing rapidly rising star formation histories. Roughly 20 per cent of the population have yet more intense rest-optical nebular emission ([O III]+Hβ EW > 1000 Å), indicating an extremely young stellar population (<10 Myr) is dominating the light, as expected for systems that have undergone a recent burst of star formation. Since such extreme emission line galaxies (EELGs) are very rare at lower redshifts (Boyett et al. 2022), we lack a detailed understanding of the gas and ionizing agents in typical reionziation-era systems.

Ground-based near-infrared spectrographs offer a path towards progress at the highest redshifts, providing access to the rest-frame ultraviolet where a suite of valuable diagnostic lines are situated. The first deep spectra have revealed strong nebular emission

★ E-mail: rmainali@email.arizona.edu(RM); dpstark@arizona.edu(DPS)

from high-ionization metal species ([C III],C III]λλ1907,1909 Å, O III]λλ1660,1666 Å, C IVλλ1548,1550 Å), a significant departure from what is commonly seen at lower redshifts (Stark et al. 2015a, b, 2017; Laporte et al. 2017; Mainali et al. 2017, 2018; Hutchison et al. 2019; Topping et al. 2021). The detection of these lines reveals gas under extreme ionization conditions and points to a population of intense ionizing agents, potentially active galactic nucleus in some cases (Laporte et al. 2017; Mainali et al. 2018) and low-metallicity massive stars in others (Mainali et al. 2017; Stark et al. 2017; Berg et al. 2019, 2021). The detection of C IVλλ1548,1550 Å and [C III],C III]λλ1907,1909 Å may further indicate a higher fraction of ionizing photons escape from a galaxy (Schaerer et al. 2022). While the EW distribution in the total population is still subject to limited statistics (Mainali et al. 2018), it appears that both the gas and ionizing sources at $z \gtrsim 6$ are often significantly different from that in galaxies at $z \simeq 2$–3.

The presence of strong rest-UV nebular emission in a subset of $z \gtrsim 6$ galaxies bodes well for future studies of the reionization era. For the next-generation 25–30 m ground-based optical/infrared observatories (which are limited to constraints on the rest-frame UV at $z > 6$), these lines may provide the only way in which early galaxies can be studied spectroscopically. While typically fainter than the strong lines in the rest-optical, the suite of emission lines in the far-UV provide unique diagnostic power of the ionizing spectrum and gas physical conditions (i.e, density, temperature, ionization). Meanwhile in the near-UV, the resonant nature of the nebular Mg II emission line makes it an ideal probe of the neutral gas opacity in early galaxies, potentially providing an indirect indicator of LyC leakage at $z \gtrsim 6$ (e.g. Henry et al. 2018; Chisholm et al. 2020; Izotov et al. 2022; Seive et al. 2022; Xu et al. 2022). The advantage of Mg II relative to Ly α is that it is not obscured by the neutral intergalactic medium at very high redshifts.

To ensure that the faint rest-UV spectra provide reliable physical diagnostics from these future facilities, it is important that we understand the gas conditions and stellar populations which support prominent UV line emission. With current facilities, this is most easily done at lower redshifts where rest-frame optical emission lines which constrain the gas-phase metallicity and ionization parameter are observable with ground-based facilities. Over the last few years, a wide range of observations have been conducted with the goal of better understanding the physics regulating rest-UV emission line spectra. These studies have demonstrated that prominent C III] appears to be a fairly ubiquitous feature in the rest-UV spectra of dwarf star-forming galaxies (Erb et al. 2010; Christensen et al. 2012; Stark et al. 2014; Rigby et al. 2015; Vanzella et al. 2016, 2017; Senchyna et al. 2017; Berg et al. 2018, 2022; Du et al. 2020; Mainali et al. 2020, 2022; Schmidt et al. 2021; Tang et al. 2021; Llerena et al. 2022), reflecting the large electron temperatures associated with metal-poor gas and the hard ionizing spectrum of young, low-metallicity massive stars.

Here, we seek to build on this progress, improving our understanding of the connection between UV line emission and the physical properties of the massive stars and ionized gas. Over the last decade, we have utilized a wide range of ground-based facilities [Large Binocular Telescope (LBT), Keck, Magellan] to obtain deep spectra and imaging of some of the brightest known ($g = 19$–21) $z \simeq 1.5$–3 gravitationally lensed galaxies within Sloan Digital Sky Survey (SDSS). This sample contains galaxies with a range of physical properties, including two of the brightest known systems with the large sSFR (and extreme emission lines) that are typical in the reionization era. Central to this observational campaign are newly acquired optical spectra from the Echellette Spectrograph and Imager (ESI; Sheinis et al. 2002) on the Keck II telescope (see Jones, Stark & Ellis 2018 for more details). The ESI spectra provide moderate resolution ($R = 6300$) rest-UV spectra, enabling a unique exploration of the nature of the massive stars and the physical conditions of the ionized gas. We supplement the Keck observations (nine galaxies) with optical spectra from LBT (one galaxy) and MMT (six galaxies), near-infrared spectra from Magellan, and new optical and near-infrared imaging.

The large continuum brightness of the SDSS lensed galaxies offers several distinct advantages with respect to the much fainter low-mass galaxies that are typical of cluster fields imaged by *HST* (e.g. Christensen et al. 2012; Stark et al. 2014; Vanzella et al. 2017). First, it enables improved constraints on the ionized gas physical conditions (metallicity, density, ionization parameter) through detection of the full suite of rest-optical strong emission lines as well as occasionally allowing detection of multiple temperature and density-sensitive lines, providing a more comprehensive view of the conditions in the gas and the most important factors regulating the rest-UV line spectra. Second, the large continuum S/N in the rest-UV spectra makes it possible to detect very weak rest-UV nebular lines. This enables the rest-UV lines to be characterized in individual galaxies for a wide range of gas conditions, and not only in the most extreme and metal-poor systems. This will provide a valuable control sample for our analysis, offering insight into what factors are most important in regulating rest-UV emission line spectra. This insight will be critical in assessing the feasibility of detecting and characterizing lines in the rest-frame far and near-UV with future facilities. In this paper, we will focus primarily on C III] emission, comparing measured line strengths to other empirical and model-based quantities (i.e. gas-phase metallicity, optical line ratios with the goal of understanding the factors regulating the C III] strength.

The paper is organized as follows. We present the new imaging and spectra and discuss population synthesis modelling of broad-band SEDs in Section 2. In Section 3, we provide our results on individual galaxies. We discuss implications of our spectra of a reionization-era analogue in Section 4 and summarize our findings in Section 5.

Throughout the paper, we adopt a Λ-dominated, flat universe with $\Omega_\Lambda = 0.7$, $\Omega_M = 0.3$, and $H_0 = 70\,\mathrm{km\,s^{-1}\,Mpc^{-1}}$. All magnitudes in this paper are quoted in the AB system and EWs are given in rest-frame, unless stated otherwise.

2 OBSERVATIONS AND ANALYSIS

2.1 Sample selection

The galaxies studied in this paper were originally identified using a search algorithm that identifies blue arcs surrounding red early-type galaxies in SDSS imaging as part of the Cambridge And Sloan Survey Of Wide ARcs on the skY (CASSOWARY; e.g. Belokurov et al. 2007, 2009). The most recent catalogue of CASSOWARY lensed galaxies was presented in Stark et al. (2013a) following a large spectroscopic campaign aimed at obtaining redshifts of the source and lens galaxies. The catalogue of galaxies released in Stark et al. (2013a) contains more than 50 gravitationally lensed galaxies in SDSS. Optical magnitudes of this sample are in the range $19.6 < r < 22.3$.

Here, we present the results from a large observational investment targeting 16 of these bright lensed sources with Keck, Magellan, LBT, and MMT (see Table 1). Object identifiers from the CASSOWARY survey are abbreviated as 'CSWA' in the table and subsequent discussion. A mosaic of the galaxies considered in this paper is shown in Fig. 1. In the following subsections, we describe the imaging

Table 1. Summary of rest-frame UV observations of our bright gravitationally lensed CASSOWARY galaxy sample. New ultra-deep moderate resolution optical spectra have been obtained for nine of these sources using ESI on Keck. We also include an additional seven sources from Stark et al. (2013a) with high-quality MMT blue channel spectra. From left to right, we present the object ID in the CASSOWARY catalogue, the RA and Dec., the spectroscopic redshift, apparent magnitude, the date the optical spectra were obtained, the rest-UV wavelength coverage provided by the optical spectra, the exposure time and position angle of the optical spectra, the absolute magnitude of the arc in the rest-UV, the magnification factor provided by gravitational lensing, and the optical spectrograph utilized. Further details are presented in Section 2.

Object	RA	Dec.	z_{spec}	m_{AB}	Dates	Rest-UV coverage (Å)	t_{exp} (ks)	PA (deg)	M_{UV}	μ	Instrument
CSWA-165	01:05:19.65	+01:44:56.4	2.127	21.1	2012 Dec 12	1020–2560	3.6	5.0	−22.0	5.4[a]	MMT/BCS
CSWA-116	01:43:50.13	+16:07:39.0	1.499	20.8	2011 Sept 29	1280–3200	2.7	105	−20.9	10.7[a]	MMT/BCS
CSWA-103	01:45:04.18	−04:55:42.7	1.959	22.1	2012 Nov 8–10	1350–3425	25	115	−20.9	4.7[a]	Keck/ESI
CSWA-164	02:32:49.97	−03:23:29.3	2.512	19.9	2012 Nov 8–10	1140–2880	28	158	−22.0	20.8[a]	Keck/ESI
CSWA-11	08:00:12.37	+08:12:07.0	1.409	21.1	2012 Mar 24	1330–3280	1.8	60	−22.3	1.9[c]	MMT/BCS
CSWA-139	08:07:31.51	+44:10:48.5	2.536	22.1	2012 Mar 23	905–2260	3.6	80	−20.8	3.8[a]	MMT/BCS
CSWA-141	08:46:47.53	+04:46:09.3	1.425	20.5	2012 Nov 8	1655–4180	5.2	190	−22.1	5.5[a]	Keck/ESI
–	–	–	–	–	2015 Nov 11	1440–2140	3.6	190	–	–	LBT/MODS
CSWA-19	09:00:02.64	+22:34:04.9	2.032	20.9	2012 Nov 9–10	1320–3330	20	86	−21.9	6.5[a]	Keck/ESI
CSWA-40	09:52:40.22	+34:34:46.1	2.189	21.4	2013 Mar 5–6	1255–3175	16.2	70	−22.3	3.2[a]	Keck/ESI
CSWA-2	10:38:43.58	+48:49:17.7	2.196	20.9	2013 Mar 5	1250–3125	7.2	17	−22.3	8.4[a]	Keck/ESI
CSWA-16	11:11:03.68	+53:08:54.9	1.945	22.1	2012 Mar 24	1085–2715	2.7	267	−20.8	3.9[d]	MMT/BCS
CSWA-38	12:26:51.69	+21:52:25.5	2.925	21.3	2013 Mar 6	1020–2580	10.8	130	−20.2	40[b]	Keck/ESI
CSWA-13	12:37:36.20	+55:33:42.9	1.864	20.3	2012 Mar 24	1120–2790	1.8	320	−23.0	1.9[d]	MMT/BCS
CSWA-39	15:27:45.02	+06:52:33.9	2.762	20.9	2013 Mar 5–6	1065–2695	18	105	−21.5	15[b]	Keck/ESI
CSWA-128	19:58:35.65	+59:50:53.6	2.225	20.6	2012 Nov 8–10	1240–3140	16.3	60	−21.9	10[c]	Keck/ESI
CSWA-163	21:58:43.68	+02:57:30.2	2.081	22.4	2011 Sept 30	1035–2600	1.8	20	−20.4	6.5[a]	MMT/BCS

Note. [a]Stark et al. (2013a), [b]Koester et al. (2010), [c]Leethochawalit et al. (2016), [d]This work.

and spectral data sets that we have obtained for this paper. The galaxies considered here were selected from the larger sample of Stark et al. (2013a) based on the brightness of the continuum. We also preferentially targeted sources at redshifts which place rest-optical lines in regions of significant atmospheric transmission in the near-IR.

2.2 Spectroscopy

2.2.1 Optical spectroscopy

We have acquired deep Keck/ESI optical spectra of nine galaxies from the Stark et al. (2013a) sample (see Table 1 for details), enabling robust constraints to be placed on the strength of nebular UV metal line emission. The positioning of the ESI slit on the lensed galaxies is shown in Fig. 1. The spectra were obtained in two observing runs between 2012 November and 2013 March. The ESI spectra cover observed wavelengths between 4000 and 10 100 Å, providing rest-frame spectral coverage that typically ranges between 1300 and 2000 Å (see Table 1). A slit width of 0.75 arcsec was used, providing a resolving power of $R = 6300$ (FWHM = 48 km s^{-1}). The data were reduced using the ESIRedux code written by J. X. Prochaska. Sky subtraction is performed following the bias subtraction and flat fielding. The 1D spectra are then extracted using a boxcar aperture matched to the spatial extent of the arc. When multiple lensed images appear on the slit, the traces are extracted separately and then combined to maximize the S/N. The continuum is generally well detected, with S/N $\simeq$ 10 per resolution element at 6200 Å. Example spectra are shown in Fig. 2. A full description of the ESI observations and spectral reduction is presented in Jones et al. (2018).

One source in the ESI sample, CSWA-141, was also observed with the Multi Object Double Spectrograph (MODS, Pogge et al. 2010) on the LBT. MODS provides bluer wavelength coverage than ESI, allowing constraints to be placed on emission from C IV, O III], and He II. We used a long slit of width 0.8 arcsec with the 400 lines mm^{-1} grating, providing spectral resolution of ∼3 Å.

We also include seven other galaxies from Stark et al. (2013a) for which the MMT Blue Channel Spectrograph (BCS) discovery spectra have sufficient continuum S/N to characterize the rest-UV metal emission lines. The MMT BCS data were obtained with the 300 lines mm^{-1} grating, providing total spectral coverage of ∼ 5300 Å. For the slit width of 1.0 arcsec used in the observations, the typical spectral resolution is ∼6.5 Å. More details of the MMT observations are provided in Stark et al. (2013b).

In total, the Keck, LBT, and MMT data provide rest-UV spectra for 16 galaxies. Our aim is to characterize C III] emission feature, typically the strongest rest-UV emission line, along with other rest-UV emission features in the whole sample. Using redshift presented in Jones et al. (2018) for the Keck/ESI data and in Stark et al. (2013a) for the MMT data, we first searched for C III] emission in individual galaxy spectrum. The line is spectrally resolved in the Keck spectra, whereas it remained unresolved in the MMT spectra. For the resolved C III] doublet, we measured emission-line fluxes and associated errors (for error spectrum) in individual components by directly integrating the flux levels within ±1 Å of individual line centres (rest-frame). When the line is unresolved, we computed total C III] emission-line fluxes and associated line flux errors directly from the flux spectra and error spectra, respectively. If the line remained undetected at 3σ level, we calculated upper limits by integrating error spectrum from 1905 to 1912 Å. The emission line EW is then computed by dividing the line fluxes (or upper limits) by median continuum level measured on either side of the C III] line. We then searched for any other rest-UV emission features in the spectra and characterized them when detected. Our sample includes 10 galaxies with C III] detection where the EWs range from 0.4 to 4.6 Å (see Table 2). We will come back to interpret the C III] EWs in Section 3.2, comparing the line strengths to optical line ratios and gas physical properties.

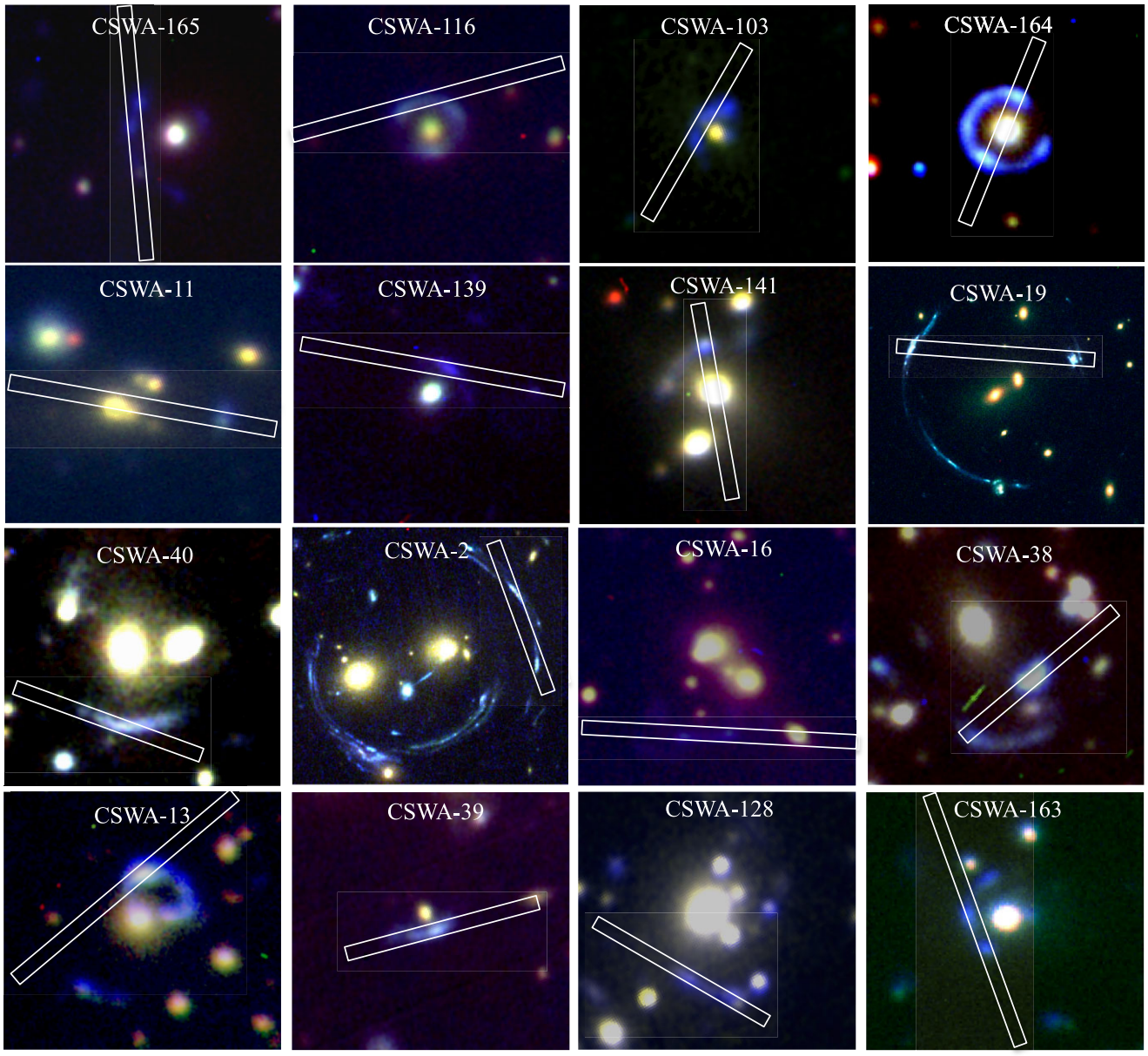

Figure 1. Colour images of 16 gravitationally lensed galaxies. The name of each sources is presented at the top of each image, along with the slit position used for the observations. For seven galaxies (CSWA-141, CSWA-13, CSWA-139, CSWA-116, CSWA-16, CSWA-165, CSWA-164) the colour images are created from *g*-, *r*-, and *i*-band images from LBT/MODS. The colour images for four galaxies (CSWA-11, CSWA-163, CSWA-128, CSWA-103) are made with *g*-, *r*- and *i*-bands images from LBT/LBC. Three colour images (CSWA-38, CSWA-39, CSWA-40) are made using Keck/ESI images in *V*, *R*, and *I* bands. For other two galaxies (CSWA-2, CSWA-19), colour images are created using archival HST images. North is up and east is to the left. Each postage stamp is 25 arcsec × 25 arcsec in size. The orientation and centroid of the ESI or MMT slit is overlaid in each image.

2.2.2 *Near-infrared spectroscopy*

Near-infrared (NIR) spectra supplement the optical spectra described above, providing constraints on the metallicity, ionization parameter, and electron density of the ionized gas. Near-infrared spectroscopic analysis is limited to the subset of sources from Table 1 which are located at redshifts placing strong rest-optical emission lines in spectral windows in which atmospheric transmission is near-unity. One of the sources in our sample (CSWA-2) was targeted with Keck near-infrared spectroscopy in Jones et al. (2013). In observing runs between 2012 November and 2015 November, we have obtained near-infrared spectroscopic observations of five additional sources (CSWA-141, CSWA-164, CSWA-165, CSWA-163, CSWA-11) using the Folded-port InfraRed Echellette (FIRE; Simcoe et al. 2008) on the Magellan Baade Telescope. We used FIRE in its echelle mode, providing continuous spectral coverage spanning 0.82–2.51 μm. We adopted a slit width of 0.75 arcsec, delivering a spectral resolution of 2.6 Å in the *J* band, 3.4 Å in the *H* band, and 4.7 Å in the *K* band. Spectroscopic data reduction was performed using standard routines in the FIREHOSE data reduction pipeline.[1]

One additional galaxy (CSWA-128) was observed on 2012 November 7 with the LUCI near-IR spectrograph on the LBT. We

[1] wikis.mit.edu/confluence/display/FIRE/FIRE+Data+Reduction

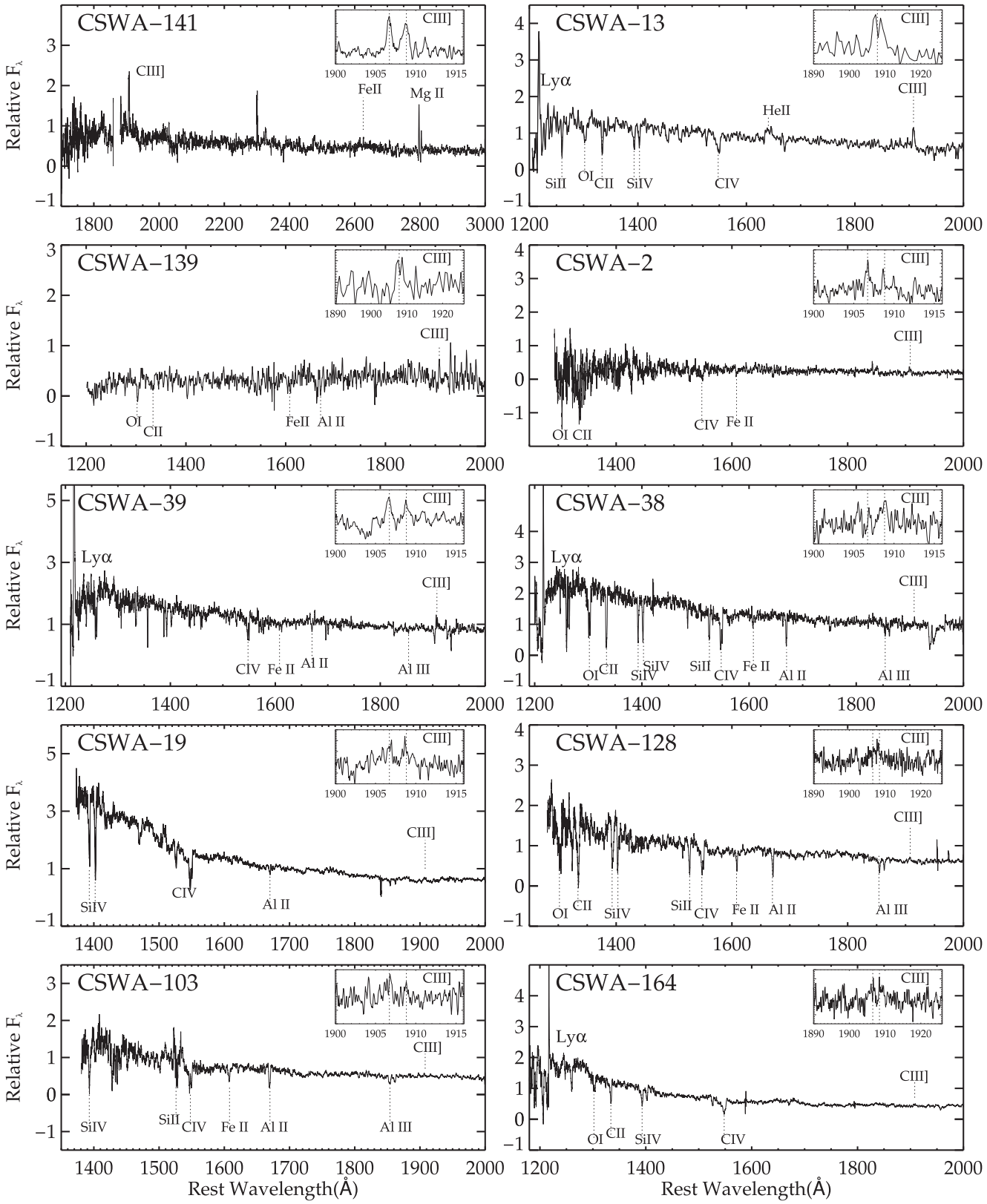

Figure 2. Rest-UV spectra of gravitationally lensed galaxies presented in Table 1 with C III] detections. The upper left side of each image contains the CASSOWARY-ID. The dot–dashed line below and above the UV continuum represents absorption and emission features identified in the spectra. The upper right of each panel shows zoom-in spectral coverage near C III]λλ1907,1909. The vertical dashed lines in the inset show the location of C III]λλ1907,1909 doublet. The C III] doublet remain unresolved in the MMT/BCS spectra of CSWA-13 and CSWA-139.

Table 2. Equivalent width measurements of rest-UV emission lines. The numbers within parentheses represent uncertainty. The upper limits are 3σ.

Object	EW (Å)			
	Ly α	[C III]λ1907	C III]λ1909	C III]λ1908 [a]
CSWA-141	–	2.3(1.3)	2.3(1.4)	4.6(1.9)
CSWA-13	5.4(2.1)	–	–	4.4(0.9)
CSWA-139	–	–	–	3.4(2.6)
CSWA-2	–	2.0(1.6)	1.1(0.9)	3.1(1.6)
CSWA-39	11.8(6.2)	0.6(0.1)	0.5(0.1)	1.1(0.2)
CSWA-19	–	0.4(0.1)	0.3(0.1)	0.7(0.1)
CSWA-38	2.6(1.1)	–	0.4(0.1)	
CSWA-128	–	0.3(0.1)	0.3(0.1)	0.6(0.1)
CSWA-103	–	0.3(0.1)	0.2(0.1)	0.5(0.1)
CSWA-164	2.0(0.5)	0.2(0.1)	0.2(0.1)	0.4(0.1)
CSWA-163	–	–	–	<3.1
CSWA-16	–	–	–	<2.3
CSWA-165	–	–	–	<1.9
CSWA-40	–	<1.2	<1.2	<1.7
CSWA-11	–	–	–	<1.4
CSWA-116	–	–	–	<1.1

Note. [a]Total C III] doublet.

Table 3. Details of near-infrared spectroscopic observations obtained for this paper. From left to right, the columns denote the object ID, observation dates, exposure time, position angle of slit, and the observatory and instrument used to acquire near-IR spectroscopy. Further details are provided in Section 2.2.

Object	Dates	t_{exp} (ks)	PA (deg)	Observatory/ Instrument
CSWA-165	2014 June 22	7.2	120	Magellen/FIRE
CSWA-164	2015 Nov 03	4.8	58	Magellen/FIRE
CSWA-11	2015 Nov 04	2.7	−10	Magellen/FIRE
CSWA-141	2012 Feb 15	1.2	280	Magellen/FIRE
CSWA-128	2012 Nov 7	3.6	190	LBT/LUCI
CSWA-163	2014 June 22	9.0	90	Magellen/FIRE

used the N1.8 camera and 200_H+K grating in longslit mode. We first observed the lensed source with the HKSpec filter centred at 1.93 microns, providing spectral coverage from 1.50 to 2.30 μm. We also observed CSWA-128 with the zJSpec filter centred at 1.1 microns, providing spectral coverage between 0.95 and 1.40 μm. A slit width of 1.0 arcsec was used, resulting in a spectral resolution of 16 Å. Spectroscopic data reduction was performed using standard IDL long slit reduction packages (see Bian et al. 2010 for details). We summarize details of near-infrared spectroscopy of CASSOWARY galaxies in Table 3. Example spectra are shown in Fig. 3.

Emission-line fluxes in the NIR spectra are measured using the IDL routine MPFITPEAK which computes line fluxes after fitting a Gaussian model. In cases where the emission lines are partially affected by a skyline, we mask the contaminated region before fitting the emission line. Additionally, if one of the components of [O III]$\lambda\lambda$4959,5007 is strongly affected by an emission line, we assume the theoretical line ratio of [O III]λ5007/[O III]λ4959 = 2.98 (Storey & Zeippen 2000) in calculating the total [O III] line flux.

We calculate the impact of dust on the nebular lines using the Balmer decrement flux ratio of Hα/Hβ. The observed line ratio is compared to the line ratio expected in absence of dust (Hα/Hβ = 2.86; Osterbrock & Ferland 2006) for case B recombination assuming T_e = 10 000 K. In the two cases where the Balmer line ratios are not available, we use the stellar reddening inferred from the broad-band data to estimate the nebular attenuation (see Section 2.5). We note that using stellar reddening for nebular attenuation correction does not impact our results. We assume that the nebular gas attenuation is similar to the stellar continuum attenuation. We presented the observed and dust-corrected emission line measurements in Table 4.

For one object (CSWA-141) where auroral [O III]λ4363 line is detected, we calculated electron temperature using PYNEB (version 1.1.8; Luridiana, Morisset & Shaw 2015) using emission-line flux ratio of O III]λ4363/[O III]λ5007. For our calculations, we adopted the default PYNEB atomic data sets. We assumed electron density of 250 cm^{-3}, which is typical to $z \sim 2$ galaxies (Sanders et al. 2016a). However, we note that our assumed electron density value has negligible effect on the derived electron temperature in the low-density regime ($<10^3$ cm^{-3}). Since we do nt have T_e([O II]) sensitive emission line measurements, we followed the relation given by Izotov et al. (2006) for low metallicity to estimate the electron temperature in the O^{+2} region. We use our electron temperature measurements to infer the direct oxygen abundance. We only use O^+/H^+ and O^{+2}/H^+ to compute oxygen abundance since the ionization states higher than O^{+2} contributes significantly low at less than 1 per cent (Izotov et al. 2006). O^+/H^+ and O^{+2}/H^+ are calculated from PYNEB using our T_e([O III], T_e([O II], n_e and emission-line fluxes of [O II], Hβ and [O III].

We use PYNEB to calculate the electron density using the flux ratio of the [O II], [S II], and [C III], C III] doublets. The typical error in measurements is then calculated using the errors in emission-line fluxes. When an electron temperature measurement is not available, we assumed electron temperature of 10 000 K following Sanders et al. (2016a) to adopt temperature-dependent effective collision strengths. Adopting electron temperature of 7000 K (15 000 K) instead would overestimate (underestimate) electron density by 15–20 per cent which is effectively lower than density error from our line flux measurements.

2.3 Imaging

Each of the CASSOWARY galaxies was discovered in SDSS imaging. In many cases, the photometric constraints from SDSS are unreliable owing to blending with neighbours and low S/N detection of diffuse emission associated with the arcs. We have obtained deeper optical multiband imaging for each of the galaxies discussed in this paper using cameras on the LBT and Keck. In order to better characterize the stellar populations, we have also obtained near-IR imaging sampling across the Balmer break for a subset of our targets using the LBT, MMT, and Keck. In the following subsections, we describe the optical and near-infrared imaging observations and analysis. Details of the new imaging observations are summarized in Table 5.

2.3.1 Optical imaging

We secured images of seven galaxies from Table 1 using the MODS (Pogge et al. 2010) on LBT in 2014 January. The dual channel mode of MODS provides images in two separate filters simultaneously over a field of view of 6 × 6 arcmin. We used the blue and red channel to obtain *g*-, *r*-, and *z*-band images for CSWA-13, CSWA-16, CSWA-116, CSWA-139, CSWA-141, CSWA-164, and CSWA-165. Each arc was first observed in the *g* and *r* band for 360 s and then in the *g* and *z* band for an additional 360 s. For one source (CSWA 16), we obtained imaging only in the *g* and *r* bands. The sky was partly covered by clouds throughout the MODS observations and the seeing varied between 1.0 and 1.5 arcsec. Optical images of three other galaxies (CSWA-39, CSWA-38, CSWA-40) were taken with ESI on Keck,

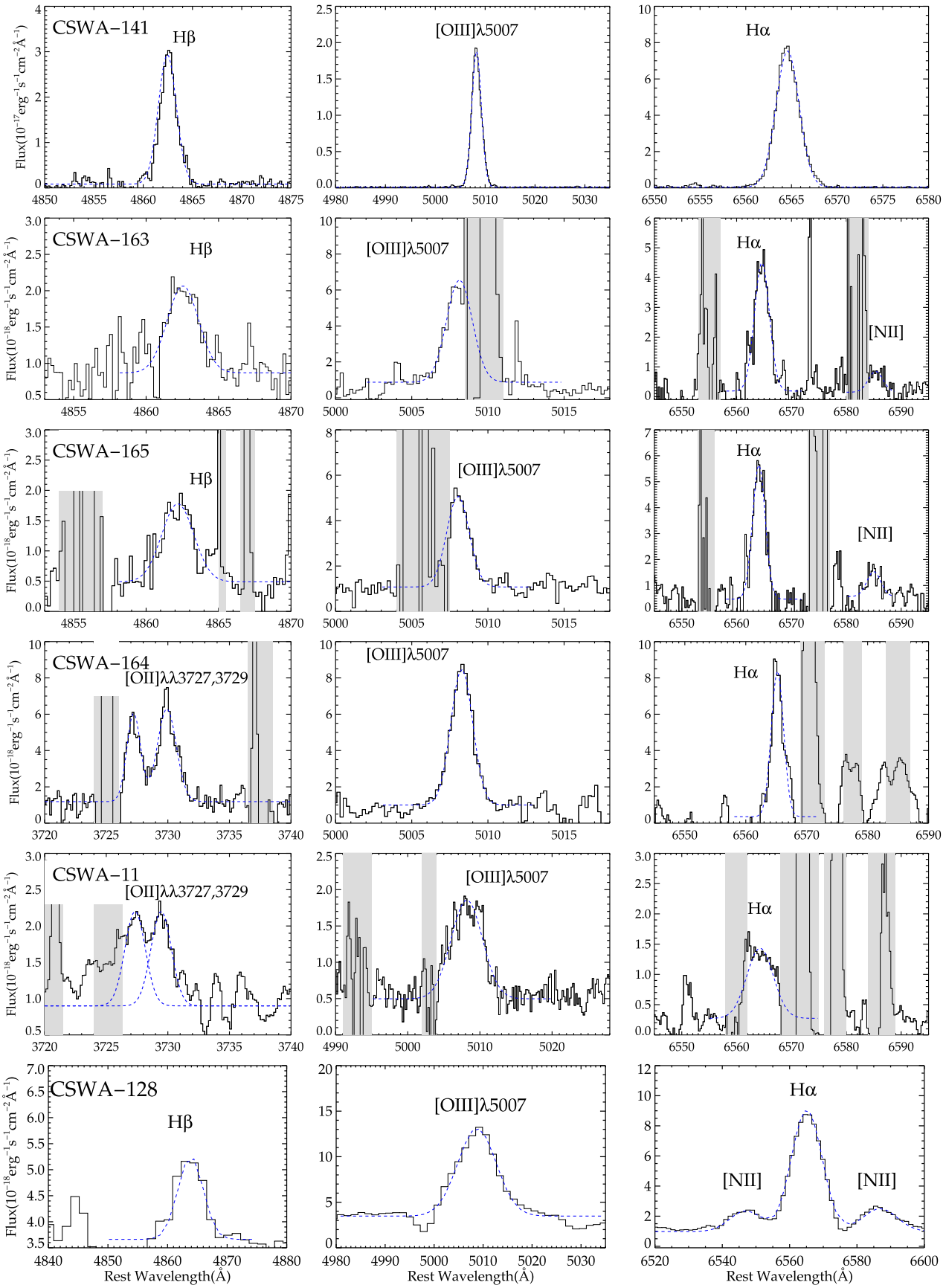

Figure 3. Optical emission lines in six gravitationally lensed galaxies discussed in this paper. Each row shows optical emission lines from a single source. The object ID is given in the leftmost panel of each row. The black line represents observed flux and the blue line shows Gaussian fit to the line profile calculated using IDL routine MPFITPEAK. The region affected by skylines is shown as a grey swath.

Table 4. Rest-optical emission line measurements of six bright lensed Cassowary galaxies. Measurements are from Magellan/FIRE (CSWA-141, CSWA-165, CSWA-163, CSWA-164, CSWA-11) and LBT/LUCI (CSWA-128). Line flux measurements are quoted relative to [O III]λ5007. We adopt [O III]λ5007 as a reference line due to its high S/N. 3σ upper limits are reported for emission lines that are not detected.

Line	λ_{rest}(Å)	λ_{obs} (Å)	F(λ)/F(5007)	I(λ)/I(5007)
		CSWA-141		
[OII]	3727.13	9039.2	0.060 ± 0.002	0.088 ± 0.003
[OII]	3729.92	9045.9	0.075 ± 0.004	0.110 ± 0.006
[NeIII]	3869.66	9384.9	0.054 ± 0.017	0.075 ± 0.023
H δ	4102.90	9950.5	0.030 ± 0.004	0.039 ± 0.005
H γ	4341.58	10529.4	0.063 ± 0.003	0.076 ± 0.004
[OIII]	4365.31	10586.9	0.019 ± 0.002	0.023 ± 0.002
H β	4862.55	11792.9	0.13 ± 0.003	0.135 ± 0.003
[OIII]	4960.25	12029.8	0.338 ± 0.004	0.342 ± 0.004
[OIII]	5008.27	12146.3	1.000	1.000
[SIII]	6310.48	15304.4	0.007 ± 0.001	0.005 ± 0.001
[NII]	6549.84	–	<0.004	<0.002
H α	6564.61	15920.7	0.529 ± 0.003	0.386 ± 0.002
[SII]	6717.96	16292.7	0.017 ± 0.001	0.013 ± 0.001
[SII]	6732.34	16327.5	0.016 ± 0.001	0.012 ± 0.001
		CSWA-165		
[OII]	3727.13	11657.1	0.56 ± 0.06	1.01 ± 0.11
[OII]	3729.92	11665.9	0.63 ± 0.08	1.13 ± 0.14
[NeIII]	3869.66	–	<0.23	<0.38
H β	4862.55	15208.9	0.46 ± 0.08	0.49 ± 0.08
[OIII]	5008.27	15665.2	1.00	1.00
H α	6564.61	20532.4	2.25 ± 0.15	1.40 ± 0.09
[NII]	6585.28	20597.5	0.55 ± 0.09	0.34 ± 0.06
		CSWA-163		
[OII]	3727.13	11482.5	0.28 ± 0.01	0.53 ± 0.02
[OII]	3729.92	11491.2	0.35 ± 0.03	0.66 ± 0.06
[NeIII]	3869.66	–	<0.04	<0.07
H γ	4341.58	13375.6	0.06 ± 0.03	0.08 ± 0.04
H β	4862.55	14981.5	0.22 ± 0.03	0.23 ± 0.03
[OIII]	4960.25	15282.5	0.35 ± 0.02	0.35 ± 0.02
[OIII]	5008.27	15429.9	1.00	1.00
H α	6564.61	20225.5	1.12 ± 0.04	0.67 ± 0.02
[NII]	6585.28	20289.2	0.18 ± 0.06	0.11 ± 0.04
		CSWA-128		
[OII]	3729.01	12019.6	0.28 ± 0.08	0.40 ± 0.11
[NeIII]	3869.66	12476. 4	0.10 ± 0.03	0.14 ± 0.04
H β	4862.55	15681.7	0.24 ± 0.06	0.25 ± 0.06
[OIII]	4960.25	15997.7	0.32 ± 0.04	0.33 ± 0.04
[OIII]	5008.27	16151.8	1.00	1.00
[NII]	6549.84	21121.3	0.05 ± 0.01	0.04 ± 0.01
H α	6564.61	21170.3	0.96 ± 0.05	0.71 ± 0.04
[NII]	6585.28	21237.2	0.13 ± 0.02	0.09 ± 0.01
[SII]	6717.96	21664.9	0.10 ± 0.02	0.07 ± 0.01
[SII]	6732.34	21711.1	0.08 ± 0.04	0.06 ± 0.02
		CSWA-164		
[OII]	3727.13	13090.9	0.52 ± 0.11	0.80 ± 0.17
[OII]	3729.92	13100.4	0.64 ± 0.04	0.99 ± 0.0.07
[OIII]	5008.27	17590.4	1.00	1.00
H α	6564.61	23064.8	1.91 ± 0.09	1.34 ± 0.06
		CSWA-11		
[OII]	3727.13	8979.9	0.67 ± 0.13	0.85 ± 0.16
[OII]	3729.92	8986.6	0.66 ± 0.09	0.83 ± 0.11
[NeIII]	3869.66	–	<0.43	<0.53
[OIII]	5008.27	12068.7	1.00	1.00
H α	6564.61	15816.5	1.08 ± 0.06	0.89 ± 0.05

Table 5. New optical and near-infrared imaging of CASSOWARY lensed galaxies obtained with Keck, LBT, and MMT. From left to right, columns denote the object ID, observatory and instrument, filters utilized, dates of observations, and exposure time.

Object	Observatory/ Instrument	Filters observed	Dates	t_{exp} (s)
CSWA-165	LBT/MODS	g	2014 Jan 27	720
	LBT/MODS	r, z	2014 Jan 27	360
	MMT/MMIRS	J	2015 Sept 30	900
	MMT/MMIRS	K	2015 Sept 30	1200
CSWA-116	LBT/MODS	g	2014 Jan 27	720
	LBT/MODS	r, z	2014 Jan 27	360
	MMT/MMIRS	J,K	2015 Oct 01	600
CSWA-103	LBT/LBC	g	2015 Nov 15	600
	LBT/LBC	r, i	2015 Nov 15	300
	MMT/MMIRS	J,K	2015 Oct 01	600
CSWA-164	LBT/MODS	g	2014 Jan 27	720
	LBT/MODS	r, z	2014 Jan 27	360
CSWA-11	LBT/LBC	g	2015 Nov 15	600
	LBT/LBC	r, z	2015 Nov 15	300
	Keck/ MOSFIRE	K_s	2015 Nov 30	300
CSWA-139	LBT/MODS	g	2014 Jan 27	720
	LBT/MODS	r, z	2014 Jan 27	360
	MMT/MMIRS	H	2017 Jan 11	900
CSWA-141	LBT/ MODS	g	2014 Jan 27	720
	LBT/ MODS	r, z	2014 Jan 27	360
	Keck/ MOSFIRE	K_s	2014 Apr 11	300
	Keck/ MOSFIRE	Y	2015 Nov 30	300
	Keck/ MOSFIRE	J2	2015 Nov 30	300
CSWA-40	Keck/ESI	V, R, I	2013 Mar 06	200
CSWA-16	LBT/MODS	g, r	2014 Jan 27	360
CSWA-38	Keck/ESI	V, R, I	2013 Mar 06	200
CSWA-13	LBT/MODS	g	2014 Jan 27	720
	LBT/MODS	r, z	2014 Jan 27	360
	LBT/LUCI	K_s	2014 Apr 13	1200
CSWA-39	Keck/ESI	V, R, I	2013 Mar 06	200
CSWA-128	LBT/LBC	g	2015 Nov 15	600
	LBT/LBC	r, i	2015 Nov 15	300
	Keck/ MOSFIRE	K_s	2014 Apr 11	300
CSWA-163	LBT/LBC	g	2015 Nov 15	600
	LBT/LBC	r, i	2015 Nov 15	300
	MMT/MMIRS	J	2015 Sept 30	900
	MMT/MMIRS	K	2015 Sept 30	1200

providing a field of view of 2 × 3.5 arcmin. These three sources were observed with V, R, and I filters. There was some cloud during the observations, and the seeing was between 0.8 and 1.2 arcsec. For the two other sources in Table 1, CSWA-2 and CSWA-19, we use archival HST images (program 11974, PI: Allam). We summarize the details of the imaging observations in Table 5.

The optical images were reduced using standard routines for flat fielding and image combination. The 5σ typical limiting magnitude in the g, r, and z bands of MODS images are 25.5, 24.7, and 23.2, respectively. Similarly, for the ESI images the typical 5σ limiting magnitude in *V*, *R*, and *I* bands are 22.7, 22.6, and 22.6, respectively. For the archival HST images, the typical 5σ limiting magnitudes in *F*450*W*, *F*606*W*, and *F*814*W* filters are 26.3, 26.1, and 25.5, respectively. Each image was flux calibrated using stars that are isolated and well detected in SDSS imaging. The mosaic in Fig. 1 shows the multicolour optical imaging obtained for each source.

Before performing photometry on the lensed galaxies, we modelled the foreground lens using GALFIT (Peng et al. 2002)

and subtracted its contribution to the lensed source. To calculate the absolute magnitude for the galaxies in our sample, we first measured the integrated flux in the g band. After applying the appropriate magnification corrections (see Section 2.4), we arrive at the absolute UV magnitudes shown in Table 1. The values span $M_{UV} = -23.1$ to $M_{UV} = -20.4$, corresponding to 0.8–9 $L^{\star}_{UV}$ at $z \simeq 2$–3 (Reddy & Steidel 2009; Parsa et al. 2016).

2.3.2 *Near-infrared imaging*

We obtained near-infrared images of CSWA-141, CSWA-11, and CSWA-128 in the K_s band using the Multi-Object Spectrometer for Infra-Red Exploration (MOSFIRE, McLean et al. 2012) on Keck I. Conditions were photometric with seeing of 0.5 arcsec. We obtained 10 dithered frames having 6.1 × 6.1 arcmin field of view, each with exposure time of 30 s. The 5σ AB limiting magnitude in the MOSFIRE K_s-band images is 23.1. With the goal of constraining the EW of [O III] and H β emission, we observed CSWA-141 with the MOSFIRE J2 medium band filter. The filter spans 1.11–1.25 μm, covering H β and [O III].

We secured a K_s-band image of CSWA-13 using the LUCI near-IR Spectrograph on the LBT when the seeing was 1.2 arcsec. We utilized the N3.75 camera providing 4 × 4 arcmin of field of view with a plate scale of 0.12 arcsec per pixel. The near-IR imaging reduction was performed using standard IDL routines designed to flat field, sky-subtract, and stack the dithered frames. Finally, we used isolated and unsaturated stars that are in the 2MASS catalogue to flux calibrate the images. The 5σ AB limiting magnitude in the LUCI K_s-band image is 23.4. For another four galaxies (CSWA-116, CSWA-165, CSWA-103, CSWA-163), near-IR imaging was obtained using the MMIRS instrument on the MMT. Each of the four sources was observed in the J and K bands. MMIRS provides imaging over a field of view of 6.9 × 6.9 arcmin with a plate scale of 0.20 arcsec per pixel. The seeing was between 0.6 and 0.9 arcsec throughout the observations. The typical 5σ AB limiting magnitude in MMIRS J- and K-band images are 22.9 and 22.8, respectively.

2.4 Lensing magnification

Derivation of stellar mass and intrinsic luminosity of lensed systems requires magnification correction. In Stark et al. (2013b), magnification factors were presented for 11 out of 16 sources given in Table 1 and typically range between $\mu = 5$ and 10. Three out of the five remaining sources have a published lens model. We adopted magnifications for CSWA-38 and CSWA-39 from Koester et al. (2010) and CSWA-11 from Leethochawalit et al. (2016).

For the two remaining sources (CSWA-13 and CSWA-16), we follow a similar approach to Hezaveh et al. (2013). In brief, we assumed a symmetric Gaussian light distribution for the lensed source. We also tested the impact of adding a second Gaussian component to the source. The foreground lens is modelled as a Singular Isothermal Ellipsoid. Multiple lenses are allowed in the modelling procedure. To obtain the best-fitting model, we perform a Markov Chain Monte Carlo analysis to minimize χ^2 in the image plane. In the case of CSWA-16, the observed data are better fit after introducing a second Gaussian component to the background source. The magnification factor is then calculated as the ratio of the lensed to unlensed flux. We derive a magnification of $\mu = 3.9 \pm 0.3$ for CSWA-16 and $\mu = 1.9 \pm 0.2$ for CSWA-13.

2.5 Stellar population synthesis modelling

13 of the galaxies shown in Fig. 1 have the necessary optical and near-IR imaging to derive physical properties from broad-band SED fitting. For these systems, we infer the stellar mass, sSFR, and dust attenuation using the Bayesian galaxy SED modelling and interpreting tool BEAGLE tool (version 0.20.3; Chevallard & Charlot 2016). BEAGLE is based on the photoionization models of star-forming galaxies in Gutkin, Charlot & Bruzual (2016), combining the latest version of the Bruzual & Charlot (2003) stellar population synthesis models with the photoionization code CLOUDY (Ferland et al. 2013).

We fit the broad-band photometric fluxes as well as C III] EWs. When relative fluxing between rest-UV and optical emission lines is possible, we include all emission lines in the fitting procedure. The models assume constant star formation where the maximum stellar age is allowed to vary freely between 5 Myr to the Universe age at the given redshift. We use Chabrier (2003) initial mass function and the Calzetti et al. (2000) extinction curve. The metallicity is allowed to vary in the range of $-2.2 \leq \log(Z/Z)_{\odot} \leq 0.25$ assuming equivalent stellar and nebular metallicity ($Z_{\star} = Z_{ISM}$). The redshift of all objects is fixed to their spectroscopic redshift given in Table 1. The ionization parameter (U_S; here defined as the ratio of ionizing-photon to gas densities at the edge of the Strömgren sphere) is varied in the range of $-4.0 \leq U_S \leq -1.0$, and the dust-to-metal mass ratio spanned within the range of $\xi_d = 0.1-0.5$. We adopt models with hydrogen density ($n_H = 100$ cm^{-3}) and C/O abundance of 0.5 of solar value [$(C/O)_{\odot} \approx 0.44$]. Finally, the prior on the V-band dust attenuation optical depths ($\hat{\tau}_V$) is taken as an exponential distribution after fixing the fraction of attenuation optical depth arising from the ambient ISM (μ) to be 0.4. We note that our assumption of constant star formation may underestimate the stellar mass by as high as 0.5 dex when the galaxy is dominated by a young stellar population, but this would not affect the primary conclusions of this paper. We discuss the main results of this SED fitting in Section 3.2.

3 RESULTS

All 16 sources presented in this paper have optical spectra covering C III] to quantify EWs. We report these values (or 3σ upper limits) in Table 2. Of the 16 sources, six galaxies have near-IR spectra enabling rest optical line flux ratios (Table 3). 10 sources have multiwavelength photometry with SED information enabling stellar mass and sSFR measurements. Below we briefly comment on individual galaxy properties where sources are ordered by descending C III] EW.

3.1 Notes on individual sources

CSWA-141 is an extreme EW optical line emitting galaxy at $z = 1.425$ with an integrated apparent magnitude of $r = 20.7$. The Magellan/FIRE spectrum reported in Stark et al. (2013a) shows a large number of rest-frame optical emission lines, including the temperature sensitive [O III]λ4363 auroral line and the density sensitive [S II]λλ6717,6731 and [O II]λλ3727,3730 lines (see Fig. 3). We have since obtained deep Keck/ESI and LBT/MODS optical spectra and optical and near-IR imaging, providing constraints on the rest-UV metal lines and the SED.

The optical to near-infrared SED of CSWA-141 (Fig. 4) implies a very large specific star formation rate (sSFR $= 31^{+61}_{-16}$ Gyr^{-1}). After correcting for magnification due to lensing ($\mu = 5.5$), the stellar mass and star formation rate of the best-fitting model are 3.98×10^8 $M_{\odot}$ and 12^{+24}_{-7} $M_{\odot}$ yr^{-1}, respectively (Table 6). The flux in the

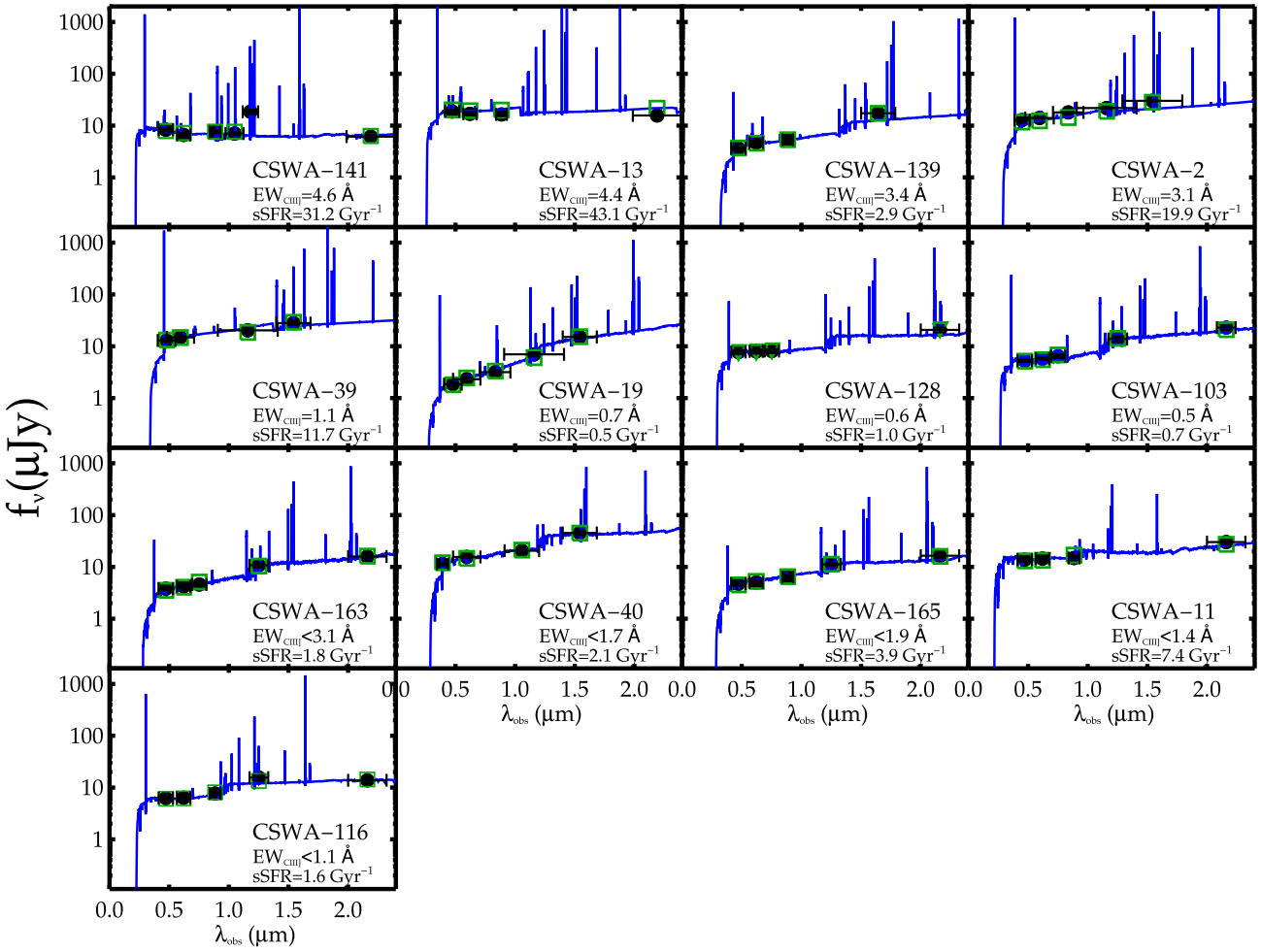

Figure 4. SEDs of galaxies in the sample. The black circle represents broad-band photometry data, the blue line represents the best-fitting population synthesis model to the observed data (see Section 2.5), and the green square shows synthetic broad-band flux from the best-fitting model. The lower right of each panel shows object ID, sSFR, and C III] equivalent widths.

Table 6. Physical properties inferred from BEAGLE fitting for subset of CASSOWARY galaxies with optical and near-IR photometry. From left to right, the columns give the object name, C III] equivalent widths, magnification-corrected stellar mass, specific star formation rates, and *V*-band optical depth.

Object	log ($M_\star/M_\odot$)	sSFR (Gyr^{-1})	$\hat{\tau}_V$
CSWA-141	$8.6^{+0.2}_{-0.3}$	$31.2^{+60.8}_{-16.3}$	$0.17^{+0.18}_{-0.12}$
CSWA-13	$9.8^{+0.3}_{-0.3}$	$43.1^{+56.6}_{-28.7}$	$0.53^{+0.13}_{-0.27}$
CSWA-139	$10.3^{+0.3}_{-0.3}$	$2.9^{+14.3}_{-2.0}$	$0.77^{+0.41}_{-0.33}$
CSWA-2	$9.1^{+0.3}_{-0.3}$	$19.9^{+26.1}_{-10.4}$	$0.96^{+0.31}_{-0.27}$
CSWA-39	$9.9^{+0.3}_{-0.4}$	$11.7^{+13.8}_{-8.1}$	$0.96^{+0.24}_{-0.31}$
CSWA-128	$9.9^{+0.1}_{-0.1}$	$1.0^{+0.4}_{-0.3}$	$0.13^{+0.06}_{-0.07}$
CSWA-19	$10.5^{+0.1}_{-0.1}$	$0.5^{+0.4}_{-0.1}$	$1.09^{+0.21}_{-0.16}$
CSWA-103	$10.4^{+0.1}_{-0.2}$	$0.7^{+1.1}_{-0.3}$	$0.48^{+0.31}_{-0.23}$
CSWA-163	$9.9^{+0.1}_{-0.1}$	$1.8^{+0.9}_{-0.9}$	$0.67^{+0.09}_{-0.13}$
CSWA-40	$10.8^{+0.2}_{-0.2}$	$2.1^{+3.3}_{-1.3}$	$0.43^{+0.29}_{-0.25}$
CSWA-165	$10.0^{+0.2}_{-0.2}$	$3.9^{+3.0}_{-1.9}$	$0.62^{+0.12}_{-0.13}$
CSWA-11	$10.0^{+0.4}_{-0.3}$	$7.4^{+14.0}_{-5.5}$	$0.28^{+0.31}_{-0.20}$
CSWA-116	$9.4^{+0.2}_{-0.2}$	$1.3^{+2.4}_{-0.7}$	$0.27^{+0.34}_{-0.18}$

medium-band J2 MOSFIRE filter (covering 1.117 to 1.246 μm) is significantly in excess of that in adjacent filters, as expected given the contamination by extremely strong [O III] and H β lines. We use the J2 flux excess to calculate the EW from [O III] and H β, following the methodology adopted at higher redshift (e.g.Stark et al. 2013b; Smit et al. 2015). This approach yields a rest-frame EW of $W_{[O\,III]+H\,\beta}$ =730 Å, consistent with the very young stellar populations (32 Myr for constant star formation) implied by the population synthesis modelling. While the optical line EW is significantly in excess of what is seen in typical star-forming galaxies at $z \simeq 2$ (e.g. Boyett et al. 2022), it is nearly identical to the average [O III]+H β EW at $z \simeq$ 7–8, as implied by flux excesses in *Spitzer*/IRAC bandpasses (Labbé et al. 2013; Smit et al. 2015; De Barros et al. 2017; Endsley et al. 2021). The continuum brightness of CSWA-141 enables a unique and detailed view of this population.

The ESI spectrum covers 4100–10 000 Å, revealing prominent emission from [C III]λ1907, C III]λ1909, Fe II*λ2626, Mg IIλλ2797,2804, [O II]λλ3726,3729, [Ne III]λ3869, and Hδ (Table 7). The [C III], C III] doublet is easily resolved by ESI (Fig. 2) with a total rest-frame EW of $W_{C\,III]}$ = 4.6 Å, the largest of the 16 galaxies considered in this paper. Nebular Mg II emission also exhibits a very large rest-frame EW ($W_{Mg\,II}$ = 15.0 Å), as is common in lower mass galaxies (e.g. Erb et al. 2012; Guseva et al.

Table 7. Rest-UV emission line measurements of CSWA-141. Emission-line fluxes are presented relative to the C III]λ1909 line flux for the Keck/ESI data, while the line fluxes are presented relative to unresolved combined C III] flux for LBT/MODS data. The upper limits are 3σ.

Line	λ_{rest} (Å)	λ_{obs} (Å)	$\frac{F_{line}}{F_{CIII]1909}}$	EW (Å)
		Keck/ESI		
[C III]	1906.73	4624.32	1.02(0.10)	2.3(1.3)
C III]	1908.68	4628.84	1.00	2.3(1.4)
Fe II*	2626.64	6370.24	0.22(0.07)	0.9(0.5)
Mg II	2796.36	6783.42	1.30(0.07)	9.7(6.8)
	2803.53	6800.79	0.65(0.04)	4.8(2.6)
[OII]	3727.10	9039.02	5.10(0.04)	26.3(12.4)
	3729.86	9045.68	6.62(0.09)	39.2(19.9)
[NeIII]	3870.16	9385.28	4.79(0.23)	19.5(13.8)
		LBT/MODS		
Line	λ_{rest} (Å)	λ_{obs} (Å)	$\frac{F_{line}}{F_{CIII]1908}}$	EW (Å)
[C III]	1908	4622.13	1.00	3.5(1.5)
He II	1640.52	3974.16	<0.08	<0.7
C IV	1549	3758.75	<0.11	<0.8
O III]	1660.81	4027.93	0.09(0.02)	0.3(0.2)
	1666.15	4040.15	0.23(0.03)	0.7(0.2)
Si III]	1882.98	4566.25	0.24(0.03)	0.7(0.1)
Si III]	1892.03	4588.16	0.11(0.02)	0.3(0.1)

2019). The MODS spectrum provides better blue sensitivity than ESI, yielding detection of O III]λ1661,1666 and Si III]λλ1883,1892. The C III] doublet is also detected, but it is unresolved at the resolution of MODS (Fig. 5). The summed EWs of the O III] and Si III] doublet (1.0 and 1.0 Å, respectively) are considerably lower than C III] (see Table 7). The high-ionization lines He IIλ1640 and C IVλλ1548,1550 are not detected, implying rest-frame EWs below 0.3 and 0.5 Å (at 3σ), respectively. For emission lines detected by both ESI and MODS, we will adopt whichever instrument provides the higher S/N EW measurement for our subsequent analysis and discussion.

The rest-frame optical emission lines detected in the FIRE spectrum provide an array of constraints on the nebular gas physical conditions. The detection of [O III]λ4363 in the FIRE spectrum enables a measure of the nebular electron temperature (T_e = 1.5 ± 0.1 × 10^4 K) and the oxygen abundance via the direct T_e method. Following the process discussed in Section 2.2.2, we find that 12 + log(O/H) = 7.95 ± 0.08, implying a gas-phase metallicity of 0.18 $Z_\odot$. Our measurement is very similar to Sanders et al. (2016b) who reported oxygen abundance (12 + log(O/H)) of CSWA-141 based on our line flux measurements given in Table 4. The derived metallicity is also consistent with the metallicities derived from the N2 and O3N2 indices with the calibration presented in Bian, Kewley & Dopita (2018) (12 + log(O/H) < 8.0).

The O32 (6.6) and R_{23} indices (11.4) point to a large ionization parameter and gas excitation. The exact values depend on the input ionizing spectrum. Photoionization modelling using BEAGLE resulted in a large ionization parameter of log $U_s = -2.1 \pm 0.1$, which is broadly consistent with O_{32} versus ionization parameter relationships in the literature (e.g. Sanders et al. 2016a; Berg et al. 2019). The photoionization modelling further suggested a high ionizing photon production efficiency of log (ξ_{ion}/Hz erg^{-1}) = 25.5 ± 0.1. This is higher than the canonical value typically assumed for galaxy-driven reionization model (Robertson et al. 2010) but consistent with other strong C III] emitters in the literature (e.g. Nakajima et al. 2018). While the measured O_{32} and R_{23} are rare among more massive star-forming galaxies at $z \simeq 2$, they are consistent with the O_{32}-sSFR and O_{32}-R_{23} trends that are observed at high redshift (e.g. Sanders et al. 2016a; Strom et al. 2017).

The electron densities inferred from the flux ratios of the [O II] and [S II] doublets using PYNEB (160^{+76}_{-74} cm^{-3} and 350^{+294}_{-206} cm^{-3}, respectively) are consistent with the median density of more massive star-forming galaxies at $z \simeq 2$ (250 cm^{-3}; e.g. Sanders et al. 2016a). In contrast, the resolved [C III], C III] doublet suggests gas at very high density ($16\,500^{+12\,100}_{-7800}$ cm^{-3}). Such an offset between densities derived from C III] and those inferred from [O II], [S II] have been seen in other galaxies at high redshift (e.g. James et al. 2014). We will come back to discuss this in more detail in Section 4.

Finally, we note that the MODS and FIRE spectra reveal emission lines at 3827, 15 304, 15 612, 15 763, and 20 663 Å, which appear nearly spatially coincident with CSWA-141 but are not associated with the $z = 1.425$ galaxy (see Fig. 5). We identify these as Lyα, Hβ, [O III]λλ4959,5007, and Hα in a second fainter gravitationally lensed source at $z = 2.148$. This higher redshift galaxy is unresolved from the $z = 1.425$ source in existing ground-based optical and near-infrared images. Given that the Hα flux of the $z = 1.425$ galaxy is 7.4× larger than the $z = 2.148$ source, we expect that the newly discovered higher redshift source contributes negligibly (at the 5 per cent level) to the broad-band flux and the rest-UV continuum in the MODS and ESI spectra. Higher resolution imaging will be required to disentangle the two sources.

CSWA-13 is a bright galaxy at $z = 1.87$ that was first confirmed in Stark et al. (2013a) through the detection of Lyα emission and numerous interstellar absorption lines in an MMT blue channel spectrum. C III] emission is confidently detected ($W_{C\,III]} = 4.4 \pm 0.9$ Å) in the discovery spectrum. He II is also detected ($W_{He\,II} = 4.3 \pm 0.9$ Å) with a broad FWHM (2430 km s^{-1}) that is indicative of a stellar wind origin. We do not detect the O III] doublet, implying individual components with EWs less than 0.8 Å. While this is among the strongest C III] emitters in our sample, the redshift places the strong rest-optical lines in regions of poor atmospheric transmission. We have obtained multiwavelength imaging in the optical and near-IR (Fig. 4). The SED reveals a large sSFR (43.1 Gyr^{-1}), little dust attenuation ($\hat{\tau}_V$=0.53), and a magnification-corrected stellar mass of log ($M_\star/M_\odot$) = 9.8.

CSWA-139 was confirmed to have a redshift of $z = 2.54$ in Stark et al. (2013a) based on the presence of Lyα absorption and interstellar metal absorption lines in an MMT spectrum. The spectrum also shows emission from the [C III],C III]λλ1907,1909 doublet with a total EW of $W_{C\,III]} = 3.4 \pm 2.6$ Å. Here, we present new optical and near-IR imaging from the LBT and MMT. The SED is best fit with an sSFR of 2.9 Gyr^{-1}, $\hat{\tau}_V$=0.77, and a stellar mass of log ($M_\star/M_\odot$) = 10.3 after magnification correction.

CSWA-2 (SDSS J1038+4849) was first reported in Belokurov et al. (2009), and the source redshift ($z = 2.20$) was subsequently confirmed in Jones et al. (2013) through detection of rest-optical emission lines. The lens reconstruction described in Jones et al. (2013) shows that CSWA-2 is a merger of two systems with a stellar mass ratio (6 ± 3):1. log ($M_\star/M_\odot$) = $9.1^{+0.2}_{-0.1}$ and one of the largest sSFR (19.9 Gyr^{-1}). The oxygen abundance 12+log(O/H) of the system as calculated using N2 index is 8.25 (∼0.4 $Z_\odot$). The Balmer decrement ratio (Hα/Hβ = 3.47) suggests little nebular extinction, whereas O3 of 1.80 imply relatively larger excitation from ionized gas. Using the metallicity calibration of Bian et al. (2018), we estimate the oxygen abundance 12+log(O/H) of the system using the O3 index as 8.4 (∼0.5 $Z_\odot$) In this paper, we present new optical spectroscopy of this system obtained with ESI. The spectrum is dominated by continuum emission from the lower

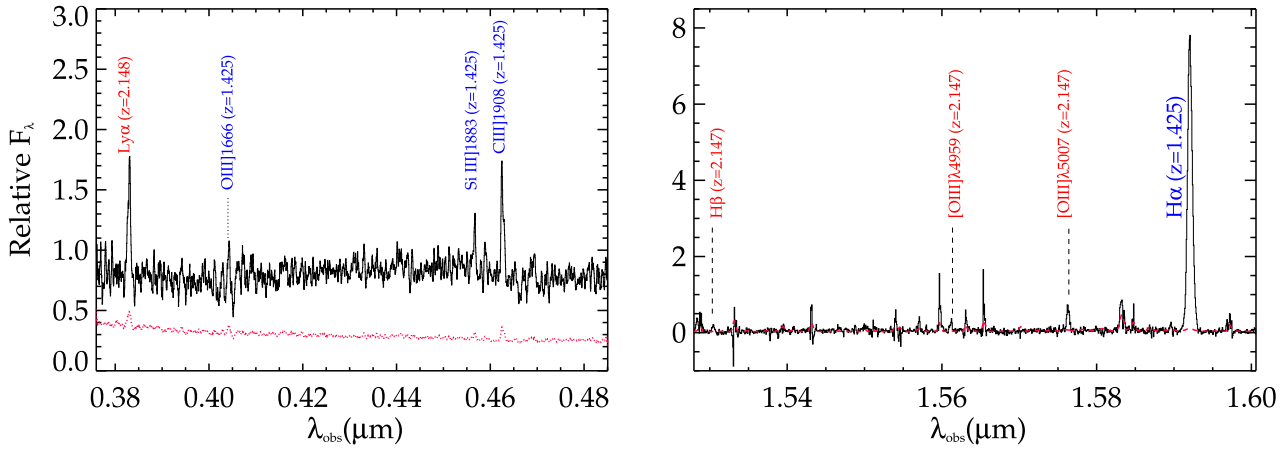

Figure 5. Optical and NIR spectra of CSWA-141. A secondary source (CSWA-141b) is identified in the Optical+NIR spectra (see Section 3) (Left:) Ly α emission at $z = 2.148$ from CSWA-141b in the LBT/MODS spectrum alongside [Si III]λ1883 and C III]λ1908 from CSWA-141 at $z = 1.425$. (Right:) Rest optical lines ([O III]$\lambda\lambda$4959,5007, H β) from CSWA-141b at $z = 2.147$ observed in the FIRE spectrum alongside the H α emission line from CSWA-141.

mass source (denoted J1038 North in Jones et al. 2013) which is considerably brighter in the optical. The spectrum shows emission from [C III],C III]$\lambda\lambda$1907,1909 with a total EW of $W_{C\,III]}$=3.1 $\pm$ 1.8 Å.

CSWA-39 (SDSS J1527+0652), a bright ($r = 20.5$) $z = 2.759$ galaxy was first identified as part of the SDSS Giant Arcs Survey (SGAS; Hennawi et al. 2008) and was spectroscopically confirmed by Koester et al. (2010) through detection of Ly α emission and interstellar absorption lines. We have obtained an ESI optical spectrum and multicolour optical imaging. Both components of the [C III], C III] doublet are detected in the spectrum, with a total S/N = 16.1 for the summed doublet flux. The rest-frame EW ($W_{C\,III]}$ = 1.1 Å) is typical of similarly luminous galaxies at this redshift (e.g. Shapley et al. 2003; Du et al. 2017). We also detect Ly α emission with a moderate rest-frame EW ($W_{Ly\,\alpha} = 11.8 \pm 6.2$ Å). No other nebular UV lines are detected in the ESI spectrum. The upper limit on the O III]$\lambda\lambda$1661,1666 components imply EWs below 1 Å, consistent with the O III] emission strengths in the Shapley et al. (2003) composite of $z \simeq 3$ galaxies with similar Ly α EWs.

CSWA-38 (SDSS J1226+2152) was confirmed to lie at $z = 2.923$ by detection of Ly α and metal absorption lines in Koester et al. (2010). Like CSWA-39, this source was first identified in Sloan Giant Arcs survey. Here, we present deep ESI spectroscopy and imaging. The optical spectrum reveals a 4.1σ detection of the C III]λ1909 component, but the [C III]λ1907 component is situated on a skyline, precluding a useful limit. The rest-frame EW of the C III]λ1909 component ($W_{C\,III]\lambda1909} = 0.4$ Å) is comparable to CSWA-38 and CSWA-19. Ly α emission is weak ($W_{Ly\,\alpha} = 0.4$ Å), and no other nebular UV lines are detected.

CSWA-19 (SDSS J0900+2234) was first confirmed in Diehl et al. (2009) at $z = 2.03$ via detection of Ly α emission and several metal absorption features in a spectrum from the dual imaging spectrograph (DIS) on the Astrophysical Research Consortium (ARC) 3.5 m telescope at the Apache Point Observatory. We have since obtained a deep ESI spectrum and MMT near-infrared imaging of this source. The combined optical and near-infrared SED is best fit by a model with a (magnification-corrected) stellar mass of log ($M_\star/M_\odot$) = 10.5, an sSFR of 0.5 Gyr^{-1}, and V-band attenuation optical depth of $\hat{\tau}_V$= 1.09. The ESI spectrum of the source shows weak detections of [C III], C III] $\lambda\lambda$1907, 1909 with an integrated S/N = 8.6 across both components of the doublet. The total rest-frame EW ($W_{C\,III]} = 0.7$ Å) is among the lowest in our sample. No other nebular rest-UV lines are detected, as Ly α is situated to the blue of the ESI coverage.

CSWA-128 (SDSS J1958+5950) is a bright ($r = 20.7$) $z = 2.22$ galaxy that was spectroscopically confirmed in Stark et al. (2013a) through detection of rest-optical emission lines in an LBT/LUCI near-infrared spectrum and interstellar metal absorption lines in an MMT optical spectrum. We have since obtained optical and near-infrared imaging and a deep ESI optical spectrum. The magnification-corrected SED (Fig. 4) implies a stellar mass of log ($M_\star/M_\odot$) = $9.9^{+0.3}_{-0.3}$ and an sSFR of 1.0 Gyr^{-1}. The ESI spectrum reveals a faint 4.8σ detection of [C III], C III] emission at the systemic redshift (z = 2.225) defined by the rest-optical lines, implying a rest-frame EW of $W_{C\,III]} = 0.7$ Å for the doublet. No other nebular lines are detected in the rest-UV.

The flux ratios of rest-optical lines (Table 4) constrain the gas physical conditions, providing a framework to understand the weak UV nebular line emission. We infer the gas-phase oxygen abundance using the R23, O32, and O3 calibration presented in Bian et al. (2018). The three indices suggest metallicities of 12+log O/H = 8.2 (O32), 12+log O/H=8.4 (R23), and 12+log O/H=8.5 (O3). As discussed in Sanders et al. (2020), O32 metallicity calibration in Bian et al. (2018) may provide a better estimate of oxygen abundance for high-redshift galaxy. This suggests that the metallicity of the ionized gas of CSWA-128 is ~0.3–0.4 $Z_\odot$. The values of O32 (3.3) and R23 (7.0) are a factor of 2.0 and 1.6 smaller than that of the strong C III] emitter CSWA-141, consistent with expectations for nebular gas with a lower ionization parameter and excitation. In contrast, the electron density implied by the [S II]$\lambda\lambda$6717,6731 doublet (200 cm^{-3}) is similar to that found in both strong C III] emitters such as CSWA-141 and typical $z \simeq$ 2–3 galaxies (Sanders et al. 2016a).

CSWA-103 (SDSS J0145-0455) is a $z = 1.96$ galaxy that was confirmed in Stark et al. (2013a) through detection of metal absorption lines and weak Ly α emission in an MMT blue channel spectrum. We have since obtained a moderate resolution Keck/ESI spectrum and optical and near-infrared imaging with LBT and MMT, respectively. The broad-band SED (Fig. 4) is best fit by a stellar synthesis model with a stellar mass (magnification-corrected) of log ($M_\star/M_\odot$) = 10.4, sSFR = 0.7 Gyr^{-1}, and $\hat{\tau}_V = 0.48$. The ESI spectrum constrains rest-frame wavelengths 1350–3425 Å. Positive emission is detected from both components of the [C III], C III] doublet, implying a total rest-

frame EW of 0.5 Å. No other nebular emission lines are observed in the ESI spectrum.

CSWA-164 (SDSS J0232-0323) was spectroscopically confirmed in Stark et al. (2013a) based on the presence of Ly α emission and interstellar absorption lines in an MMT blue channel spectrum. Stark et al. (2013a) also presented detection of [O II], [O III]λ5007, and H α in a Magellan/FIRE near-infrared spectrum of CSWA-164, revealing a systemic nebular redshift of $z = 2.512$. We have since obtained a deep moderate resolution optical spectrum with ESI and optical broad-band imaging. The ESI spectrum reveals the Ly α emission ($W_{Ly\alpha} = 2.0$ Å) detected previously together with weak emission (S/N = 4.1) from the [C III],C III]$\lambda\lambda$1907,1909 doublet. This corresponds to a total C III],C III] EW of just 0.4 Å, the smallest measured value in our sample.

The FIRE spectrum provides insight into the ionized gas physical conditions of CSWA-164. Unfortunately both H β and [N II] are obscured by skylines, precluding a robust determination of the oxygen abundance through standard strong line calibrations. We can however estimate oxygen abundance using O32 metallicity calibrations from Bian et al. (2018). We find that O32 = 0.7 corresponds to the oxygen abundance of 12+log O/H = 8.6. Thus, the ionized gas appear to be reasonably metal rich in CSWA-164. The value of ionization-sensitive line ratios (O32 = 0.7) is among the lowest in our sample. In contrast to the metallicity and ionization parameter, the electron density derived from the [O II] doublet (165 cm^{-3}) is consistent with the range spanned by other galaxies in our sample.

CSWA-40 (SDSS J0952+3434) is a $z = 2.190$ galaxy identified through the Sloan Bright Arcs Survey and spectroscopically confirmed by Kubo et al. (2010) using the DIS on the ARC 3.5 m and the RC Spectrograph on the Mayall 4 m telescope at Kitt Peak National Observatory. The spectra reveal Ly α in absorption along with several other metal absorption lines. We have obtained a moderate resolution optical spectrum and imaging with Keck/ESI. The continuum S/N of the CSWA-40 ESI spectrum is lower than other systems. This is the only ESI spectrum that does not reveal detection of the [C III], C III] doublet, implying a rest-frame EW below 1.6 Å for the sum of both components. No other nebular emission lines are observed in the spectrum.

CSWA-163 (SDSS J2158+0257) was spectroscopically confirmed in Stark et al. (2013a) based on identification of metal absorption lines and Ly α absorption in an MMT blue channel spectrum. A Magellan/FIRE near-infrared spectrum was also obtained in that paper, revealing a systemic nebular redshift of $z = 2.079$ based on detection of [O II], Hγ, H β, [O III], H α, and [N II]. We have obtained new optical and near-infrared imaging of this source, allowing constraints to be placed on the broad-band SED (Fig. 4). The data are best fit by stellar synthesis models with stellar mass log $(M_\star/M_\odot) = 9.9^{+0.1}_{-0.1}$ after magnification correction, *V*-band attenuation optical depth of $\hat{\tau}_V = 0.67$, and an sSFR of 1.8 Gyr^{-1}, suggesting CSWA-163 is a relatively massive galaxy with a fairly evolved stellar population. Perhaps not surprisingly given the low sSFR and lack of Ly α emission, the MMT blue channel spectrum does not show any C III] emission at the systemic redshift. The 3σ flux upper limit suggests that the rest-frame EW of the double must be lower than 3.1 Å.

The FIRE spectrum provides useful constraints on the ionized gas of CSWA-163. The oxygen abundance can be derived from O32 and O3 calibration from Bian et al. (2018). Both suggest moderately enriched gas: 12 + log O/H = 8.5 (O32) and 12 + log O/H = 8.4 (O3) implying a nebular oxygen abundance of 0.4–0.5 $Z_\odot$. The ionization-sensitive line ratios (O32 = 1.1, O3 = 4.3) are consistent with a relatively low-ionization parameter and moderate gas-excitation. The electron density inferred from [O II] is 144 cm^{-3}, consistent with the other systems studied in this paper.

CSWA-16 (SDSS J1111+5308) was confirmed to have a redshift of $z = 1.95$ based on the presence of numerous metal absorption lines in an MMT blue channel spectrum (Stark et al. 2013a). The discovery spectrum shows no emission from the blended [C III], C III] doublet. The 3σ upper limit on the total flux from the doublet requires the rest-frame EW to be smaller than 2.3 Å. We have obtained multiband optical imaging with LBT, allowing more robust constraints to be placed on the apparent magnitude ($r = 21.8$) and the magnification-corrected UV absolute magnitude ($M_{UV} = -20.8$).

CSWA-165 (SDSS J0105+0144) is a $z = 2.13$ galaxy that was first confirmed in Stark et al. (2013b) through detection of strong metal absorption lines and weak Ly α emission in an MMT blue channel spectrum. We have since obtained a Magellan/FIRE near-infrared spectrum and optical and near-infrared imaging from LBT and MMT, respectively. The FIRE spectrum reveals detection of [O II], H β, [O III]λ5007, H α, and [N II], indicating a systemic redshift of $z = 2.128$. The MMT shows no emission from the [C III], C III] doublet at the systemic redshift. The 3σ upper limit on the flux of the doublet indicates that the total C III] EW must be lower than 1.3 Å. The broad-band SED is best fit by a synthesis model with stellar mass of $\log(M_\star/M_\odot) = 10.0$, sSFR of 3.9 Gyr^{-1}, and $\hat{\tau}_V$=0.62.

The gas-phase metallicity can be inferred from O32, R23, and O3 strong line calibrations. All three indicate metal-rich ionized gas: 12+log O/H = 8.4 (O32) 8.6 (R23), 8.6 (O3), consistent with a gas-phase metallicity in the range 0.5–0.8 $Z_\odot$. The ionization-sensitive ratios (O32 = 0.6, O3 = 2.1) suggest an ionization parameter that is lower than average among $z \simeq$ 2–3 galaxies. In contrast, the electron density derived from the [O II] doublet flux ratio (220 cm^{-3}) is similar to that found in other systems at high redshift.

CSWA-11 (SDSS J0800+0812) was confirmed at $z = 1.41$ via detection of metal absorption lines and [O II] emission in MMT blue and red channel spectra (Stark et al. 2013a). The C III] doublet is not detected in either the blue or red channel MMT spectra, implying a rest-frame EW below 0.9 Å at 3σ. We have obtained multiwavelength imaging and near-infrared spectroscopy. The magnification-corrected SED suggests a stellar mass of $\log(M_\star/M_\odot) = 10.0^{+0.4}_{-0.3}$, an sSFR of 7.4 Gyr^{-1}, and *V*-band attenuation optical depth of $\hat{\tau}_V = 0.28$. The FIRE spectrum reveals detections of [O II], [O III]λ5007, and H α, but strong skylines obscure detections of H β, [O III]λ4959, and [N II]λ6586. Using the theoretically expected flux ratio of [O III]λ5007/[O III]λ4959, we infer that this system has O32 = 0.92, relatively low for our sample. Using the O32 calibration, we estimate metallicity of 12 + log O/H = 8.5. The electron density implied by the [OII] doublet flux ratio is 469^{+416}_{-238} cm^{-3}, consistent with the range spanned by other galaxies in our sample.

CSWA-116 (SDSS J0143+1607) is a $z = 1.50$ galaxy confirmed in Stark et al. (2013a) through detection of rest-UV metal absorption lines and [O II] in MMT blue and red channel spectra. We do not detect the C III] doublet in the MMT spectra, indicating that the rest-frame EW is below 0.7 Å at 3σ. We have obtained optical and near-infrared imaging of CSWA-116, providing constraints on the broad-band SED. The data are best fit by a stellar model with $\log(M_\star/M_\odot) = 9.4$, an sSFR of 1.3 Gyr^{-1}, and *V*-band attenuation optical depth of $\hat{\tau}_V = 0.27$.

3.2 Physical properties of CASSOWARY galaxy sample

The data obtained for this paper provide new constraints on the ionized gas properties and the stellar populations of lensed galaxies

Table 8. Rest-optical emission line properties of galaxies at high redshift with C III] emission constraints. The upper half shows data from this paper, whereas the lower half shows measurements from the literature.

Object	$EW_{CIII]}$ (Å)	R23	O32	O3	Electron density (cm^{-3})	12 + log (O/H)	Reference
CSWA-141	4.6 ± 1.9	11.4 ± 1.0	6.6 ± 1.0	7.4 ± 0.2	160^{+76}_{-74} [a], 350^{+294}_{-206} [b], 16500^{+12100}_{-7800} [c]	7.95 ± 0.08[d]	This work
CSWA-2	3.1 ± 1.6	–	–	5.2 ± 2.1	–	8.4 ± 0.2[g]	This work, 16
CSWA-128	0.7 ± 0.1	7.0 ± 1.2	3.3 ± 0.8	4.0 ± 1.1	198^{+85}_{-76} [b]	8.2 ± 0.2[e], 8.4 ± 0.2[f], 8.5 ± 0.2[g]	This work
CSWA-164	0.4 ± 0.1	–	0.7 ± 0.2	–	165^{+65}_{-46} [a]	8.6 ± 0.2[e]	This work
CSWA-163	<3.1	10.9 ± 1.1	1.1 ± 0.1	4.3 ± 0.6	144^{+45}_{-33} [a]	8.5 ± 0.2[e], 8.4 ± 0.2[g]	This work
CSWA-165	<1.9	7.1 ± 1.3	0.6 ± 0.1	2.1 ± 0.4	221^{+75}_{-64} [a]	8.4 ± 0.2[e], 8.6 ± 0.2[f], 8.6 ± 0.2[g]	This work
CSWA-11	<1.4	–	0.8 ± 0.2	–	469^{+120}_{-156} [a]	8.5 ± 0.2[e]	This work
RXCJ0232-588	21.7	6.0	9.4	4.1	80[a]	7.61 [d]	1
Ion2	18	–	>15	14.7	–	8.07[h]	2
860_359	12.4	<9.2	>6.91	6.0	–	<8.1[f]	3
ID14	11.8	<11.7	>10	7.6	–	<7.8[d]	4
SL2S0217	11.7	–	–	3.1	300[c]	7.5[d]	5
SGAS J1050+0017	11	11.4	9.7	7.9	2–3 × 100[a]	>8.1[d]	6
ID11	11	<11.8	>10	8.4	–	7.7[d]	7
CSWA-20	9.1	7.7	5.6	4.9	276[a], 17100[b]	7.82[d]	8
BX418	7.1	<9.2	>11.6	6.4	–	7.8[d]	9
A1689 31.1	7	7.8	8.2	4.7	330[a], 2900[c]	7.76[d]	10
MACS 0451–1.1	6.7	<5.9	>8.4	3.9	–	<8.0[f]	3
SDSS J1723+3411	4.0	8.6	5.5	5.4	47[a], 1950[c]	8.4[f]	11
MACS 0451–3.1	2.4	–	>2.0	–	–	–	3
Cosmic Horseshoe	0.9	5.5	1.31	2.4	840–6900[b]	8.65[f]	1213
MS 1512-cB58	0.8	7.9	1.36	3.6	–	8.47[f]	1415

Notes. [a]Derived from [O II] doublet, [b]Derived from [S II] doublet, [c]Derived from C III] doublet.
[d]Direct (T_e) method, [e]O32 method, [f]R23 method, [g]O3 method,
[h] Using HII-CHI-mistry code (Perez-Montero 2014)
[1] Mainali et al. (2020),[2]de Barros et al. (2016),[3] Stark et al. (2014),[4]Vanzella et al. (2017),[5]Berg et al. (2018),[6]Bayliss et al. (2014),[7]Vanzella et al. (2016),[8]James et al. (2014), [9]Erb et al. (2010),[10]Christensen et al. (2012), [11]Rigby et al. (2021), [12]Quider et al. (2009), [13]Hainline et al. (2009), [14]Pettini et al. (2000), [15]Teplitz et al. (2000), [16]Jones et al. (2013)

at $z \simeq 1$–3 identified by the CASSOWARY selection in SDSS. Here, we briefly describe what these data reveal about the average properties in this sample, providing a concise summary of the source-by-source description presented in Section 3.1. Following correction for magnification, the rest-frame UV absolute magnitudes are found to range between $M_{UV} = -20.2$ and $M_{UV} = -23.0$, with a median value ($M_{UV} = -21.9$) that is roughly three times the value of $L^{\star}_{UV}$ at $z \simeq 2$ (e.g. Reddy & Steidel 2009). Both optical and near-infrared imaging exist for 11 of the 16 galaxies considered in this paper, allowing the stellar content to be characterized through SED fitting. The median stellar mass and sSFR of this subset is 1.3×10^{10} $M_{\odot}$ and 2.1 Gyr^{-1}, respectively. The latter is similar to the average sSFR of $z \simeq 2$–3 galaxies (e.g. Reddy & Steidel 2009).

Rest-optical line measurements exist for seven of the CASSOWARY galaxies shown in Fig. 1. The median gas-phase oxygen abundance derived from the rest-optical line ratios is 12 + log O/H = 8.33, i.e. ionized gas metallicity of 0.4 $Z_{\odot}$. The ionization-sensitive ratio O32 ranges between 0.7 and 6.7 with a median value of O32 = 1.1. While this is slightly lower than the median O32 in the KBSS and MOSDEF surveys, it is well within the range spanned by galaxies in these samples (e.g. Sanders et al. 2016a; Steidel et al. 2016; Strom et al. 2017). The Balmer decrements range between H α/H β = 3.47 and 4.97. The median electron density derived from the [O II] or [S II] doublet flux ratios (198 cm^{-3}) is close to the average electron density of $z \simeq 2.3$ galaxies from the MOSDEF survey (Sanders et al. 2016a).

All 16 galaxies in our sample have constraints on rest-UV line emission. Most sources show very weak [C III], C III] emission. The median EW for the summed doublet is 1 Å, similar to that seen in composite spectra of $z \simeq 3$ LBGs (Shapley et al. 2003; Llerena et al. 2022). The two strongest [C III], C III] emitters (CSWA 141, CSWA −13) have rest-frame EWs of 4.6 and 4.4 Å, respectively. The rest-UV spectrum of CSWA-141 also shows prominent nebular emission from O III], Si III], and Mg II. While these lines are absent in CSWA-13, its spectrum does reveal broad He II emission, indicative of a significant Wolf Rayet population. No high-ionization nebular lines are detected in our sample.

Our sample allows to compare and contrast ISM conditions expected in strong and weak C III] emitters. A typical C III] EWs of star-forming galaxies at $z \sim 2$–3 is ∼1.7 Å (Shapley et al. 2003; Du et al. 2017). From here on, we refer to those galaxies with C III] EWs >2 × typically seen at $z \sim 2$–3 ($\gtrsim$3.5 Å) as strong C III] emitters, whereas objects with C III] EWs below this threshold are described as weak C III] emitters. Together with galaxies presented in this paper, we compile sources from the literature having constraints from both C III] EWs and optical spectra. The majority of the literature objects are lower redshifts galaxies (Giavalisco, Koratkar & Calzetti 1996; Leitherer et al. 2011; Berg et al. 2016, 2019; Senchyna et al. 2017, 2019; Ravindranath et al. 2020), while majority of sample at $z > 1$ are comprised of gravitationally lensed systems (Pettini et al. 2000; Teplitz et al. 2000; Hainline et al. 2009; Quider et al. 2009; Erb et al. 2010; Christensen et al. 2012; Jones et al. 2013; Bayliss et al. 2014; James et al. 2014; Stark et al. 2014; de Barros et al. 2016; Vanzella et al. 2016, 2017; Berg et al. 2018; Mainali et al. 2020; Rigby et al. 2021). We present a compilation of $z > 1$ sources in Table 8.

In Fig. 6, we plot empirical relationships between C III] EW and oxygen abundance (left panel), and C III] EW and O32 (right

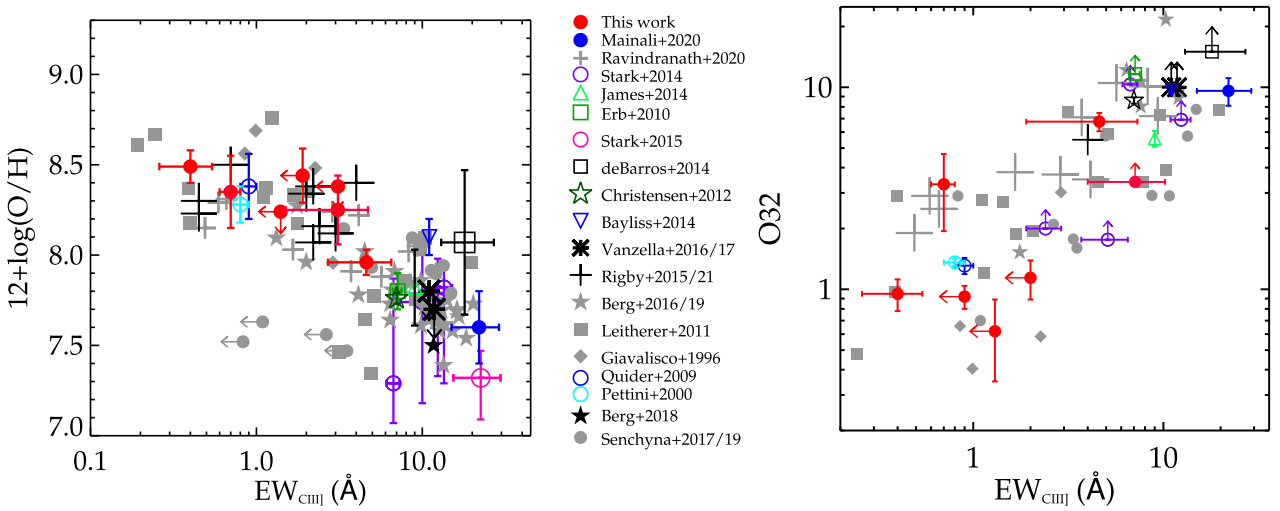

Figure 6. (Left:) Empirical relationship between oxygen abundance (12+log(O/H)) and rest frame C III] equivalent width (EW$_{CIII]}$). (Right:) Empirical relationship between the line ratio of [O III]λλ4959,5007 to [O II]λλ3727,3729 (i.e. O32) and rest-frame C III] EW (EW$_{CIII]}$). The red symbol represents bright lensed galaxies presented in this paper, while the other data points are compilation from the literature.

panel). The oxygen abundance of the strong C III] emitters are mostly measured using direct metallicity measurements, while strong optical line calibrations are used for the weaker C III] emitters (see Table 8). As can be seen in the Fig. 6, the gas-phase metallicity of the strong C III] emitters is consistently below 12 + log(O/H) = 8.0, suggesting metallicities below 20 per cent $Z_{\odot}$. In contrast, most of the weaker C III] emitters imply higher metallicities than this value. This result is consistent with previous investigations in the literature (e.g. Rigby et al. 2015; Jaskot & Ravindranath 2016; Maseda et al. 2017; Nakajima et al. 2018; Schaerer et al. 2018; Senchyna et al. 2019; Du et al. 2020; Ravindranath et al. 2020; Tang et al. 2021). The right panel of Fig. 6 shows that the O32 values of the stronger C III] emitters ($\gtrsim$3.5 Å) are on an average six times larger than the those of the weaker C III] emitters. The median O32 value of the weaker C III] emitters are similar to typical galaxies at $z \sim 2$–3 (O32 = 1.3, Sanders et al. 2016a). A variety of factors can influence the O32 value of a galaxy. The elevated values seen in the strongest of C III] emitters tend to be found in galaxies dominated by the light of a very young stellar population (Sanders et al. 2020; Tang et al. 2021), as expected in galaxies undergoing a burst of star formation. Overall, these empirical relationships support a physical picture where galaxies with metal-poor gas and young stellar populations are able to power strong C III] emission (e.g. Stark et al. 2014; Rigby et al. 2015; Senchyna et al. 2017). The scatter seen in the C III] EW at a given metallicity or O32 value may stem from differences in ISM conditions (relative carbon abundances (C/O), ionization parameters) and stellar age and metallicity.

The compilation of strong C III] emitters further provides information on the global spectral properties expected from typical reionization era systems. In Fig. 7, we show strong C III] emitters (denoted by red square) and weak C III] emitters (denoted by blue square) in log([O III]/H β) versus sSFR (left panel) and log(O32) versus log(R23) (right panel) plots. We compare them to typical line ratios expected at $z \sim 2$ using data set from KBSS survey (Steidel et al. 2014; Strom et al. 2017) and MOSDEF survey (Sanders et al. 2016a), as well as at $z \sim 0$ (local SDSS galaxies). The strong C III] emitting galaxies appear to be distinct from local SDSS galaxies as well as typical galaxies at $z \sim 2$ in both the plots. However, the position of weaker C III] emitters on both the diagrams is similar to typical galaxies at $z \sim 2$. Taken together, this further demonstrates that strong C III] emitters show highly ionized gas conditions from a large sSFR systems. Assuming these strong C III] emitters representative of a typical reionization era systems, we might expect a similar ISM conditions in galaxies at $z > 6$.

4 DISCUSSION

In this paper, we present spectra of some of the brightest-known gravitationally lensed galaxies at $z \simeq 2$–3, discovered over the footprint of SDSS. Included in this sample are CSWA-13 and CSWA-141, two exceptionally bright systems with sSFRs (>20 Gyr^{-1}) that are similar to those of the reionization era. Their spectra reveal rest-frame C III] EWs more than twice what is typical at $z \simeq 2$–3 (e.g. Shapley et al. 2003; Du et al. 2018; Llerena et al. 2022). In this section, we explore the ionized gas conditions and the properties of the outflowing gas, taking advantage of emission and absorption lines that are often too faint to be detected in individual high-redshift galaxies with similarly intense emission lines. Our analysis will primarily focus on CSWA-141, as the redshift of CSWA-13 places the strong rest-optical lines in regions of low atmospheric transmission. For CSWA 141, the rest-optical lines are similar in EW to those found in the reionization era (e.g. De Barros et al. 2017; Endsley et al. 2021; Boyett et al. 2022), classifying this galaxy as an EELG and revealing a stellar population dominated by a recent burst or upturn in star formation.

The gas properties in such intense line-emitting galaxies have been the subject of a number of spectroscopic investigations in recent years. These studies demonstrate that the nebular gas is generally under extreme ionization conditions in EELGs (Tang et al. 2019), with the ionization parameter reaching its largest values in the galaxies powered by the youngest stellar populations (or the largest EW rest-optical nebular lines). The gas in CSWA-141 is consistent with this picture, showing a large O32 ratio (6.7) as expected given its elevated sSFR (31.2 Gyr^{-1}) and [O III]+H β EW (730 Å). Its large ionization parameter implied by the photoionizaiton models (log U = −2.1) suggests a large photon density is impingent on the ionized gas. This can be driven be a variety of factors, including efficient ionizing photon production (e.g. Chevallard et al. 2018; Tang et al.

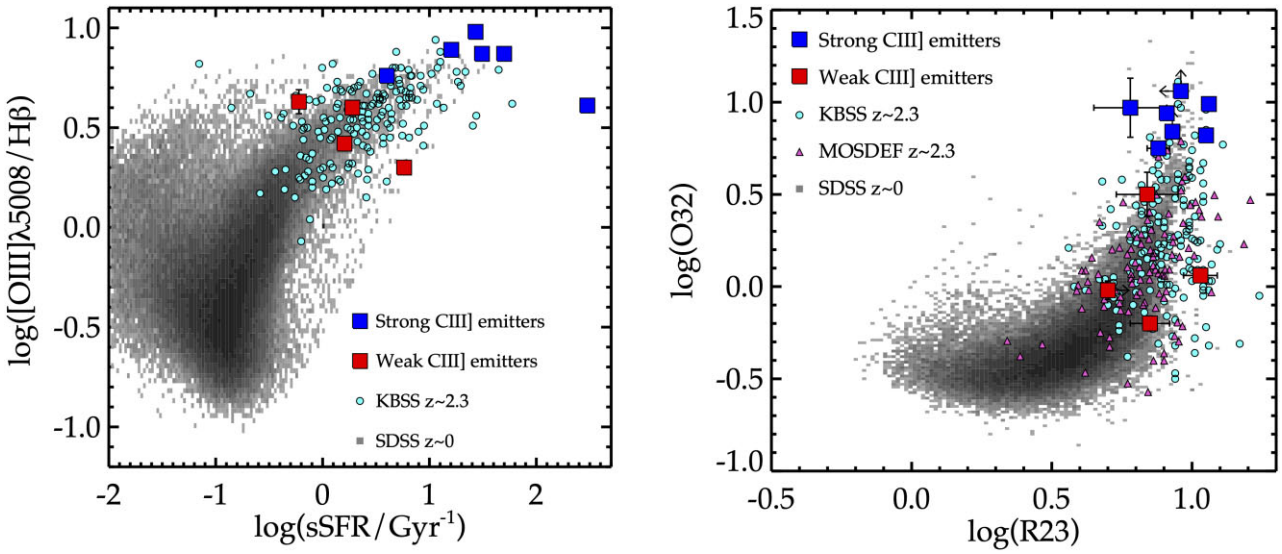

Figure 7. The strong (blue) and weak (red) C III] emitters (see Section 3.2) in O3 versus sSFR (left) and O32 versus R23 (right) plots. Star-forming galaxies at $z \sim 2.3$ from KBSS survey (Strom et al. 2017) are shown in cyan circle, whereas MOSDEF survey (Sanders et al. 2016a) are shown in violet triangle. Local galaxies from SDSS survey are shown in grey. Galaxies with properties similar to those at z>6 tend to have strongest C III] emission.

2021) and a compact configuration of ionized gas around the sources of ionizing radiation. The latter is the norm for galaxies dominated by very young stellar clusters (e.g. Whitmore et al. 2011; Hannon et al. 2019; Chen et al. 2023), and thus may be expected in EELGs like CSWA-141.

Further insight into the gas conditions of EELGs is made possible by detection of three density-sensitive emission lines in CSWA-141. As we discussed in Section 3.1, the [C III], C III] doublet implies very high gas densities ($16\,500^{+12\,100}_{-7800}$cm^{-3}), perhaps again reflecting a very compact or concentrated gas geometry surrounding the extremely young star clusters that power EELGs. Although the uncertainty in C III] density is currently large, such high densities are routinely seen in $z \simeq 2$–4 galaxies with spectrally resolved C III] measurements (e.g. Christensen et al. 2012; Bayliss et al. 2014; James et al. 2014, 2018; Acharyya et al. 2019) and are also starting to be seen in the first handful of $z \gtrsim 7$ galaxies with C III] doublet measurements (Stark et al. 2017; Jiang et al. 2021). As such, the high C III] density is less likely due to a statistical fluctuation, although a larger sample should confirm this. In most of the cases, the C III] density is also significantly in excess of that inferred from lower ionization species. The same trend is apparent in CSWA-141, with the C III] density being nearly two orders of magnitude higher than those derived from [S II] and [O II]. This is consistent with a picture (e.g. Acharyya et al. 2019; Kewley et al. 2019; Berg et al. 2021) dictated by the ionization structure of the nebulae, with the lower ionization rest-optical lines (i.e. [O II] and [S II]) probing primarily the outer layers which are preferentially dominated by lower density gas. The higher ionization lines (like C III]) probe the inner regions of the nebula, where densities are expected to be higher. Variations in the critical density of the ions will additionally contribute to C III] probing higher density gas than [O II] (e.g. James et al. 2018). A key question is whether very young EELGs like CSWA-141 (and many of the $z > 7$ galaxies) might have a large fraction of their ionized gas in very dense clumps, as is expected at the earliest evolutionary phases following the formation of star clusters (e.g. Rigby & Rieke 2004; Kim et al. 2018). Currently, samples with C III] densities tend to be those that have at least moderately large C III] EW, generally indicative of a relatively young stellar population. Larger C III] density samples are required to test whether the presence of very large densities is at all sensitive to the luminosity-weighted stellar population age.

CSWA 141 also provides a unique window on the kinematics and covering fraction of the outflowing gas in EELGs, a population which becomes commonplace at $z > 6$. As it is this outflowing gas which regulates the escape of ionizing radiation, systems like CSWA 141 offer potential for understanding the likely contribution of EELGs to reionization. At low redshift, Chisholm et al. (2017) and Jaskot et al. (2017) find that the most extreme [O III] emitting galaxies (the Green Peas) tend to have low outflow velocities and suggest that this is consistent with models of suppressed superwinds, where catastrophic cooling prevents the development of large-scale outflows (e.g. Silich, Tenorio-Tagle & Muñoz-Tuñón 2007; Silich & Tenorio-Tagle 2017; Gray et al. 2019). The low-ionization absorption lines in the CSWA 141 spectra are all blueshifted with respect to the systemic redshift, indicating the presence of outflows. In the ESI spectrum, we detect Fe II and Mg II absorption lines, while the MODS spectrum probes slightly bluer wavelengths, allowing detection of Al IIλ1670. The average velocity of low-ionization outflowing gas in CSWA 141 is 76 km s^{-1}. This is slightly lower than outflow velocities of 100–300 km s^{-1} that are commonly observed in galaxies at $z \sim 1$–3 (e.g. Shapley et al. 2003; Weiner et al. 2009; Steidel et al. 2010; Jones, Stark & Ellis 2012). However, given the low stellar mass of CSWA-141, the measurement is consistent with expectations from known trends between galaxy mass and outflow velocity (e.g. Martin 2005; Weiner et al. 2009; Erb et al. 2012; Chisholm et al. 2016).

The strength of the absorption lines in CSWA 141 provides insight into the opacity of neutral gas along the line of sight to the young star clusters which dominate the light. The Fe II λ2374 and Fe II λ2382 absorption lines are very weak with EWs of 0.5 and 1.5 Å, respectively. Jones et al. (2018) measured a column density N(Fe II) $= 1.5^{+0.7}_{-0.2} \times 10^{14}$ cm^{-2}, which is among the lowest of the sample. In Fig. 8, we compare these EWs with those measured from composite spectra of more typical star-forming galaxies at $1 < z < 2$ (Erb et al. 2012). As is clear in the figure, most star-forming galaxies at these redshifts show similar Fe II λ2374 and Fe II λ2382 EWs, as expected for optically thick neutral gas. In contrast, the Fe II λ2374 absorption

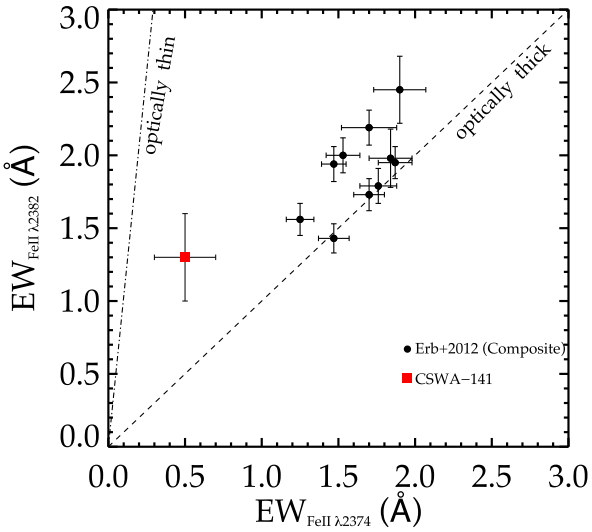

Figure 8. A comparison between EWs of Fe II λ2374 and Fe II λ2382. The red square represents CSWA-141 data point, whereas the black circles are composite data points presented in Erb et al. (2012). The two dashed black lines represent optically thin and optically thick cases. This reflects that Fe II is not optically thick in CSWA-141 and therefore has a lower column density c.f. black points.

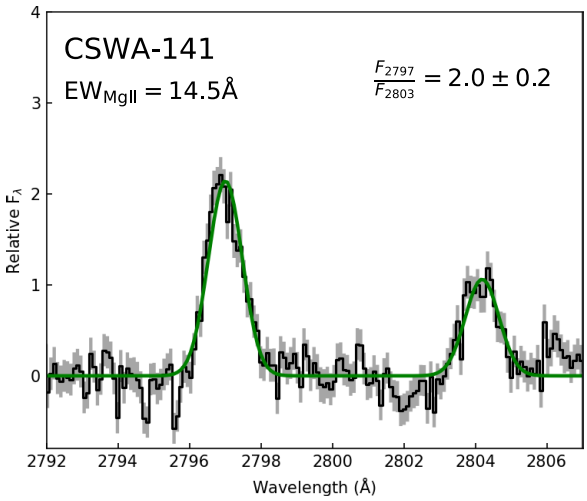

Figure 9. Mg II 27 972 803 line profile in CSWA-141. The black curve represents continuum-subtracted flux level, while the green solid line is the Gaussian fit to the observed data. Both the Mg II doublet are well fitted by a single-component Gaussian. Mg II 2797 is clearly stronger than Mg II 2803 line, suggesting a Mg II doublet intensity ratio (F_{2797}/F_{2803}) of 2.0 ± 0.2. The doublet ratio is consistent with the intrinsic recombination value (2.0) indicating minimal scattering by low-ionization ISM along the line of sight. Based on the observed Mg II doublet ratio, CSWA-141 has implied escape fraction of $f_{esc}(\mathrm{LyC}) = 27 \pm 4$ per cent.

in CSWA-141 is significantly weaker than Fe II λ2382. With an Fe II λ2374 EW that is roughly three times weaker than that found in the $z \simeq 1$–2 composites, the lines are much closer to expectations for optically thin neutral gas. We additionally note that the Fe II λ2382 line is susceptible to emission filling (e.g. Erb et al. 2012), which tends to weaken the observed Fe II λ2382 EWs. This is particularly likely to be the case for EELGs like CSWA-141. In such a scenario, the line ratio would move even closer to that expected for optically thin conditions, implying a low covering fraction and potentially low column density of neutral gas in the outflow.

Further indications that CSWA 141 has a low column density of neutral gas comes from the resonant Mg IIλλ 27 972 803 emission line. Both components of the doublet are confidently detected (S/N>10) in emission with total EWs of 14.5 Å (Fig. 9). This is not only one of the highest measured Mg II EWs at $z > 1$, but it is also one of the brightest Mg II emission lines, making detailed (and resolved) study of the line uniquely possible. Recent studies have pointed out that the flux ratio of the doublet is strongly sensitive to the neutral gas column density in the galaxy. As such it is thought to correlate closely with the ionizing photon escape fraction (Henry et al. 2018; Chisholm et al. 2020; Seive et al. 2022; Xu et al. 2022, 2023), perhaps providing one of the best indirect indicators of photon leakage. At low H I column densities ($<10^{17.2}$ cm^{-2}), galaxies become optically thin to the resonant Mg II line photons (Chisholm et al. 2020). This leads to strong nebular Mg II emission, and it drives the doublet ratio ($R = \mathrm{F}_{2797}/\mathrm{F}_{2803}$) to its intrinsic value of $R = 2$. If the line photons are resonantly scattered by Mg^+ ions in the neutral gas along the line of sight, the doublet ratio will decrease, asymptoting to a value of $R = 1$ if the gas is optically thick to Mg II photons (see Chisholm et al. 2020 for a detailed discussion).

The measured Mg II doublet ratio in CSWA-141 is $R = 2.0 \pm 0.2$, consistent with the intrinsic value produced in the H II regions. This suggests that optically thin channels along the line of sight to the young star clusters are powering the nebular emission. Both components of the doublet are well fit by single Gaussians, suggesting that the line profile is not significantly impacted by resonant scattering. The very large EW of the line also points to minimal attenuation of line photons. We note that the Mg II profile does show very weak blue-shifted absorption (see Fig. 9), suggesting the presence of some neutral gas along the line of sight, but this gas must be either optically thin or clumpy with low-density channels to result in the observed line profile.

Given the derived oxygen abundance of CSWA-141 (see Section 3.1) and nominal assumptions on the Mg/O ratio (Chisholm et al. 2020), this can be converted to an estimate of the hydrogen column density (See equation 14 of Chisholm et al. 2020). Given the measured doublet ratio is consistent with the intrinsic value, CSWA-141 is formally consistent with a negligible hydrogen column density. Within the measurement errors of the flux ratio, we find a 1σ upper limit on the H I column density of 3.8×10^{16} cm^{-2}. This value is well below the H I column density at which galaxies become optically thin to LyC radiation ($<10^{17.2}$ cm^{-2}), suggesting that CSWA-141 may be a likely candidate for LyC leakage. While more realistic geometries (i.e. clumpy gas) would alter the derived column densities, the observed line profile requires there to be low-density channels along the line of sight where resonant line photons (and potentially LyC emission) are transmitted (Gazagnes et al. 2020; Saldana-Lopez et al. 2022). Because of the extreme brightness of CSWA-141, it presents a unique opportunity to spatially resolve the absorbing gas in an extreme line emitter that is very similar in its properties to those systems at $z > 6$. An upcoming *HST* UVIS grism observations (GO-16710, PI: Mainali) will provide more direct constraints on the escape of ionizing radiation from the galaxy.

5 SUMMARY

We present new spectroscopic and photometric observations of 16 bright gravitationally lensed galaxies originally identified in SDSS via the CASSOWARY program. Observations were conducted using LBT, Keck, MMT, and Magellan. Included in this sample is the z

= 1.42 galaxy CSWA-141, one of the brightest known EELGs at high redshift, with an [O III]+Hβ EW (730 Å) nearly identical to the average value seen at $z \simeq 7$–8. In this paper, we focus on the rest-UV spectral properties of the sample, leveraging high-quality Keck/ESI data. Owing to the brightness of our targets ($g \simeq 19$–21), we are able to detect rest-UV metal line emission in the Keck spectra down to very low EW values. While most systems have weak line emission (median C III] EW =1.7 Å), CSWA 141 shows relatively strong emission (C III] EW 4.6 Å) together with detections of a variety of UV lines (O III], Si III], Fe II*, Mg II).

We compare the properties of the strong ($\gtrsim$3.5 Å) and weak ($\lesssim$3.5 Å) C III] emitters in our sample and in the literature. We find that the stronger C III] emitters have larger sSFR and lower gas-phase oxygen abundances. We find that the strong C III] emitters can be easily separated by their rest-optical line ratios, with larger values of O32 at roughly fixed R23. Overall, these results suggest that C III] tends to be strong in galaxies dominated by young stellar populations with low metallicity and extreme ionization conditions. This is consistent with trends found in observations at low and high redshift (e.g. Rigby et al. 2015; Maseda et al. 2017; Senchyna et al. 2017, 2019; Nakajima et al. 2018; Schaerer et al. 2018; Du et al. 2020; Ravindranath et al. 2020; Tang et al. 2021) and in photoionization models (e.g. Jaskot & Ravindranath 2016; Nakajima et al. 2018).

The brightness of CSWA-141 enables a detailed investigation of an EELG with properties similar to that which become common at $z > 6$. This galaxy is characterized by low stellar mass (4.0×10^8 $M_\odot$), large sSFR (31.2 Gyr^{-1}), low gas-phase metallicity (12 + log O/H = 7.95), and relatively highly ionized gas (O32 = 6.7), and has likely undergone a recent upturn or burst of star formation. We find that the electron density traced by the C III] doublet (1.65×10^4 cm^{-3}) is higher than that traced by [O II] and [S II] doublet (160 and 350 cm^{-3}, respectively), a discrepancy that is also found in other systems (e.g. James et al. 2014; Acharyya et al. 2019). While this is likely to reflect the ionization structure of the H II regions powering the lines (Kewley et al. 2019), it may also indicate that CSWA-141 contains a significant fraction of its ionized gas in very dense clumps, as is expected in the earliest stages following the formation of star clusters (e.g. Kim et al. 2018).

The spectra of CSWA-141 provide several probes of the neutral gas opacity in the galaxy, including both low-ionization absorption lines and the resolved Mg II doublet. The Fe II$\lambda\lambda$2374, 2382 absorption lines indicate the presence of outflowing gas with average velocity of 76 km s^{-1}. The lines are much weaker than in typical star-forming galaxies at $z \simeq 1$–2, implying a low covering fraction and potentially low column density of neutral gas in the outflow. The resonant Mg II$\lambda\lambda$ 27 972 803 emission line supports this picture. The Mg II doublet ratio in CSWA-141 ($R = F_{2797}/F_{2803}$) is 2.0 ± 0.2, consistent with the intrinsic value produced in the H II regions. When combined with the very large EW of Mg II and the near-Gaussian profiles of the doublet components, this suggests minimal resonant scattering, consistent with a very low column density of neutral hydrogen. These indirect indicators suggest CSWA-141 may be a likely candidate for LyC leakage.

ACKNOWLEDGEMENTS

We would like to thank Ryan Endsley for helping with MMT observations of some of the sources presented in this paper. We also thank Stephane Charlot and Jacopo Charlot for making the BEAGLE population synthesis tool available to us for this paper.

DPS acknowledges support from the National Science Foundation through the grant AST-2109066. TJ acknowledges support from the National Science Foundation through the grant AST-2108515. RSE acknowledges funding from the European Research Council (ERC) under the European Union's Horizon 2020 research and innovation 0programme (grant agreement No 669253). YH acknowledges support from the National Science and Engineering Council of Canada grant RGPIN-2020-05102, the Fonds de recherche du Québec grant 2022-NC-301305, and the Canada Research Chairs Program.

Observations presented in this paper were obtained from the Keck Observatory, which was made possible by the generous financial support of the W. M. Keck Foundation. The material is based upon work supported by NASA under award number 80GSFC21M0002. The authors acknowledge the very significant cultural role that the summit of Mauna Kea has always had within the indigenous Hawaiian community. We are most fortunate to have the opportunity to conduct observations from this mountain. Some of the observations reported here were obtained at the MMT Observatory, a joint facility of the University of Arizona and the Smithsonian Institution. This paper includes data gathered with the 6.5 m Magellan Telescopes located at Las Campanas Observatory, Chile. Some of the data presented in this paper were obtained using the LBT. The LBT is an international collaboration among institutions in the United States, Italy, and Germany. The LBT Corporation partners are: The University of Arizona on behalf of the Arizona university system; Istituto Nazionale di Astrofisica, Italy; LBT Beteiligungsgesellschaft, Germany, representing the Max Planck Society, the Astrophysical Institute Potsdam, and Heidelberg University; The Ohio State University; The Research Corporation, on behalf of The University of Notre Dame, University of Minnesota and University of Virginia.

DATA AVAILABILITY

The data underlying this article will be shared on reasonable request to the corresponding author.

REFERENCES

Acharyya A. et al., 2019, MNRAS, 488, 5862
Bayliss M. B., Rigby J. R., Sharon K., Wuyts E., Florian M., Gladders M. D., Johnson T., Oguri M., 2014, ApJ, 790, 144
Belokurov V. et al., 2007, ApJ, 671, L9
Belokurov V., Evans N. W., Hewett P. C., Moiseev A., McMahon R. G., Sanchez S. F., King L. J., 2009, MNRAS, 392, 104
Berg D. A. et al., 2022, ApJS, 261, 31
Berg D. A., Chisholm J., Erb D. K., Skillman E. D., Pogge R. W., Olivier G. M., 2021, ApJ, 922, 170
Berg D. A., Erb D. K., Auger M. W., Pettini M., Brammer G. B., 2018, ApJ, 859, 164
Berg D. A., Erb D. K., Henry R. B. C., Skillman E. D., McQuinn K. B. W., 2019, ApJ, 874, 93
Berg D. A., Skillman E. D., Henry R. B. C., Erb D. K., Carigi L., 2016, ApJ, 827, 126
Bian F. et al., 2010, ApJ, 725, 1877
Bian F., Kewley L. J., Dopita M. A., 2018, ApJ, 859, 175
Bouwens R. J. et al., 2014, ApJ, 793, 115
Bouwens R. J. et al., 2015, ApJ, 803, 34
Bouwens R. J. et al., 2021, AJ, 162, 47
Boyett K. N. K., Stark D. P., Bunker A. J., Tang M., Maseda M. V., 2022, MNRAS, 513, 4451
Bruzual G., Charlot S., 2003, MNRAS, 344, 1000
Calzetti D., Armus L., Bohlin R. C., Kinney A. L., Koornneef J., Storchi-Bergmann T., 2000, ApJ, 533, 682
Chabrier G., 2003, PASP, 115, 763

Chen Z., Stark D. P., Endsley R., Topping M., Whitler L., Charlot S., 2023, MNRAS, 518, 5607
Chevallard J. et al., 2018, MNRAS, 480, 2593
Chevallard J., Charlot S., 2016, MNRAS, 462, 1415
Chisholm J., Orlitová I., Schaerer D., Verhamme A., Worseck G., Izotov Y. I., Thuan T. X., Guseva N. G., 2017, A&A, 605, A67
Chisholm J., Prochaska J. X., Schaerer D., Gazagnes S., Henry A., 2020, MNRAS, 498, 2554
Chisholm J., Tremonti C. A., Leitherer C., Chen Y., Wofford A., 2016, MNRAS, 457, 3133
Christensen L. et al., 2012, MNRAS, 427, 1953
Curtis-Lake E. et al., 2016, MNRAS, 457, 440
de Barros S. et al., 2016, A&A, 585, A51
De Barros S. et al., 2017, A&A, 608, A123
Diehl H. T. et al., 2009, ApJ, 707, 686
Du X. et al., 2018, ApJ, 860, 75
Du X., Shapley A. E., Martin C. L., Coil A. L., 2017, ApJ, 838, 63
Du X., Shapley A. E., Tang M., Stark D. P., Martin C. L., Mobasher B., Topping M. W., Chevallard J., 2020, ApJ, 890, 65
Endsley R., Stark D. P., Chevallard J., Charlot S. , 2021, MNRAS, 500, 5229
Erb D. K., Pettini M., Shapley A. E., Steidel C. C., Law D. R., Reddy N. A., 2010, ApJ, 719, 1168
Erb D. K., Quider A. M., Henry A. L., Martin C. L., 2012, ApJ, 759, 26
Ferland G. J. et al., 2013, Rev. Mex. Astron. Astrophys., 49, 137
Finkelstein S. L. et al., 2015, ApJ, 810, 71
Gazagnes S., Chisholm J., Schaerer D., Verhamme A., Izotov Y., 2020, A&A, 639, A85
Giavalisco M., Koratkar A., Calzetti D., 1996, ApJ, 466, 831
González V., Bouwens R., Illingworth G., Labbé I., Oesch P., Franx M., Magee D., 2014, ApJ, 781, 34
Gray W. J., Oey M. S., Silich S., Scannapieco E., 2019, ApJ, 887, 161
Grazian A. et al., 2015, A&A, 575, A96
Guseva N. G., Izotov Y. I., Fricke K. J., Henkel C., 2019, A&A, 624, A21
Gutkin J., Charlot S., Bruzual G., 2016, MNRAS, 462, 1757
Hainline K. N., Shapley A. E., Kornei K. A., Pettini M., Buckley-Geer E., Allam S. S., Tucker D. L., 2009, ApJ, 701, 52
Hannon S. et al., 2019, MNRAS, 490, 4648
Hennawi J. F. et al., 2008, AJ, 135, 664
Henry A., Berg D. A., Scarlata C., Verhamme A., Erb D., 2018, ApJ, 855, 96
Hezaveh Y. D. et al., 2013, ApJ, 767, 132
Hutchison T. A. et al., 2019, ApJ, 879, 70
Ishigaki M., Kawamata R., Ouchi M., Oguri M., Shimasaku K., Ono Y., 2018, ApJ, 854, 73
Izotov Y. I., Chisholm J., Worseck G., Guseva N. G., Schaerer D., Prochaska J. X., 2022, MNRAS, 515, 2864
Izotov Y. I., Stasińska G., Meynet G., Guseva N. G., Thuan T. X., 2006, A&A, 448, 955
James B. L. et al., 2014, MNRAS, 440, 1794
James B. L., Auger M., Pettini M., Stark D. P., Belokurov V., Carniani S., 2018, MNRAS, 476, 1726
Jaskot A. E., Oey M. S., Scarlata C., Dowd T., 2017, ApJ, 851, L9
Jaskot A. E., Ravindranath S., 2016, ApJ, 833, 136
Jiang L. et al., 2021, Nat. Astron., 5, 256
Jones T., Ellis R. S., Richard J., Jullo E., 2013, ApJ, 765, 48
Jones T., Stark D. P., Ellis R. S., 2012, ApJ, 751, 51
Jones T., Stark D. P., Ellis R. S., 2018, ApJ, 863, 191
Kewley L. J., Nicholls D. C., Sutherland R., Rigby J. R., Acharya A., Dopita M. A., Bayliss M. B., 2019, ApJ, 880, 16
Kim J.-h. et al., 2018, MNRAS, 474, 4232
Koester B. P., Gladders M. D., Hennawi J. F., Sharon K., Wuyts E., Rigby J. R., Bayliss M. B., Dahle H., 2010, ApJ, 723, L73
Kubo J. M. et al., 2010, ApJ, 724, L137
Labbé I. et al., 2013, ApJ, 777, L19
Laporte N., Nakajima K., Ellis R. S., Zitrin A., Stark D. P., Mainali R., Roberts-Borsani G. W., 2017, ApJ, 851, 40
Leethochawalit N., Jones T. A., Ellis R. S., Stark D. P., Richard J., Zitrin A., Auger M., 2016, ApJ, 820, 84
Leitherer C., Tremonti C. A., Heckman T. M., Calzetti D., 2011, AJ, 141, 37
Livermore R. C., Finkelstein S. L., Lotz J. M., 2017, ApJ, 835, 113
Llerena M. et al., 2022, A&A, 659, A16
Luridiana V., Morisset C., Shaw R. A., 2015, A&A, 573, A42
Mainali R. et al., 2018, MNRAS, 479, 1180
Mainali R. et al., 2020, MNRAS, 494, 719
Mainali R. et al., 2022, ApJ, 940, 160
Mainali R., Kollmeier J. A., Stark D. P., Simcoe R. A., Walth G., Newman A. B., Miller D. R., 2017, ApJ, 836, L14
Martin C. L., 2005, ApJ, 621, 227
Maseda M. V. et al., 2017, A&A, 608, A4
McLean I. S. et al., 2012, in Proc. SPIE Conf. Ser. Society of Photo-Optical Instrumentation Engineers (SPIE) Conference Series., eds McLean I.S., Ramsay S.K., Takami H., 8446, 84460J, Ground-Based and Airborne Instrumentation for Astronomy IV. SPIE
McLure R. J. et al., 2013, MNRAS, 432, 2696
Nakajima K. et al., 2018, A&A, 612, A94
Osterbrock D. E., Ferland G. J., 2006, Astrophysics of Gaseous Nebulae and Active Galactic Nuclei, University Science Books, Sausalito, CA, United States
Parsa S., Dunlop J. S., McLure R. J., Mortlock A., 2016, MNRAS, 456, 3194
Peng C. Y., Ho L. C., Impey C. D., Rix H.-W., 2002, AJ, 124, 266
Pettini M., Steidel C. C., Adelberger K. L., Dickinson M., Giavalisco M., 2000, ApJ, 528, 96
Pogge R. W. et al., 2010, in McLean I. S., Ramsay S. K., Takami H., eds, Proc. SPIE Conf. Ser. Vol. 7735, Ground-based and Airborne Instrumentation for Astronomy III. SPIE, Bellingham, p. 77350A
Quider A. M., Pettini M., Shapley A. E., Steidel C. C., 2009, MNRAS, 398, 1263
Ravindranath S., Monroe T., Jaskot A., Ferguson H. C., Tumlinson J., 2020, ApJ, 896, 170
Reddy N. A., Steidel C. C., 2009, ApJ, 692, 778
Rigby J. R. et al., 2021, ApJ, 908, 154
Rigby J. R., Bayliss M. B., Gladders M. D., Sharon K., Wuyts E., Dahle H., Johnson T., Peña-Guerrero M., 2015, ApJ, 814, L6
Rigby J. R., Rieke G. H., 2004, ApJ, 606, 237
Roberts-Borsani G. W. et al., 2016, ApJ, 823, 143
Robertson B. E., Ellis R. S., Dunlop J. S., McLure R. J., Stark D. P. , 2010, Nature, 468, 49
Rogers A. B., McLure R. J., Dunlop J. S., 2013, MNRAS, 429, 2456
Saldana-Lopez A. et al., 2022, A&A, 663, A59
Salmon B. et al., 2015, ApJ, 799, 183
Sanders R. L. et al., 2016a, ApJ, 816, 23
Sanders R. L. et al., 2016b, ApJ, 825, L23
Sanders R. L. et al., 2020, MNRAS, 491, 1427
Schaerer D. et al., 2022, A&A, 658, L11
Schaerer D., Izotov Y. I., Nakajima K., Worseck G., Chisholm J., Verhamme A., Thuan T. X., de Barros S., 2018, A&A, 616, L14
Schmidt K. B. et al., 2021, A&A, 654, A80
Seive T., Chisholm J., Leclercq F., Zeimann G., 2022, MNRAS, 515, 5556
Senchyna P. et al., 2017, MNRAS, 472, 2608
Senchyna P., Stark D. P., Chevallard J., Charlot S., Jones T., Vidal-García A., 2019, MNRAS, 488, 3492
Shapley A. E., Steidel C. C., Pettini M., Adelberger K. L., 2003, ApJ, 588, 65
Sheinis A. I., Bolte M., Epps H. W., Kibrick R. I., Miller J. S., Radovan M. V., Bigelow B. C., Sutin B. M., 2002, PASP, 114, 851
Silich S., Tenorio-Tagle G., 2017, MNRAS, 465, 1375
Silich S., Tenorio-Tagle G., Muñoz-Tuñón C., 2007, ApJ, 669, 952
Simcoe R. A. et al., 2008, in McLean I. S., Casali M. M., eds, Proc. SPIE Conf. Ser. Vol. 7014, Ground-based and Airborne Instrumentation for Astronomy II. SPIE, Bellingham, p. 70140U
Smit R. et al., 2014, ApJ, 784, 58
Smit R. et al., 2015, ApJ, 801, 122
Stark D. P., 2016, ARA&A, 54, 761
Stark D. P. et al., 2013a, MNRAS, 436, 1040
Stark D. P. et al., 2014, MNRAS, 445, 3200
Stark D. P. et al., 2015a, MNRAS, 454, 1393
Stark D. P. et al., 2015b, MNRAS, 450, 1846

Stark D. P. et al., 2017, MNRAS, 464, 469
Stark D. P., Schenker M. A., Ellis R., Robertson B., McLure R., Dunlop J., 2013b, ApJ, 763, 129
Steidel C. C. et al., 2014, ApJ, 795, 165
Steidel C. C., Erb D. K., Shapley A. E., Pettini M., Reddy N., Bogosavljević M., Rudie G. C., Rakic O., 2010, ApJ, 717, 289
Steidel C. C., Strom A. L., Pettini M., Rudie G. C., Reddy N. A., Trainor R. F., 2016, ApJ, 826, 159
Storey P.J., Zeippen C.J., 2000, MNRAS, 312, 813
Strom A. L., Steidel C. C., Rudie G. C., Trainor R. F., Pettini M., Reddy N. A. , 2017, ApJ, 836, 164
Tang M., Stark D. P., Chevallard J., Charlot S., Endsley R., Congiu E., 2021, MNRAS, 501, 3238
Tang M., Stark D., Chevallard J., Charlot S., 2019, MNRAS, 489, 2572
Teplitz H. I. et al., 2000, ApJ, 533, L65
Topping M. W., Shapley A. E., Stark D. P., Endsley R., Robertson B., Greene J. E., Furlanetto S. R., Tang M., 2021, ApJ, 917, L36
Vanzella E. et al., 2016, ApJ, 821, L27
Vanzella E. et al., 2017, ApJ, 842, 47
Weiner B. J. et al., 2009, ApJ, 692, 187
Whitmore B. C. et al., 2011, ApJ, 729, 78
Xu X. et al., 2022, ApJ, 933, 202
Xu X. et al., 2023, ApJ, 943, 94

This paper has been typeset from a TEX/LATEX file prepared by the author.